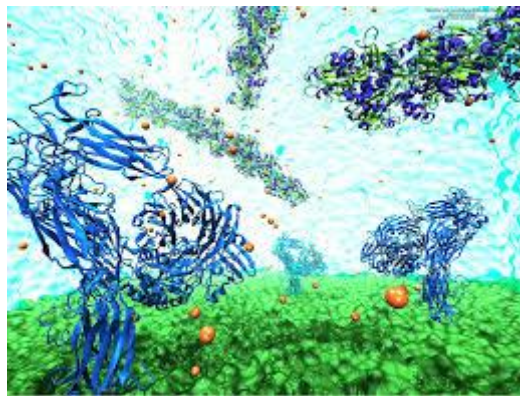


**UNIVERSITY OF CRETE**  
**BIOLOGY DEPARTMENT**  
**INSTITUTE OF MOLECULAR BIOLOGY AND BIOTECHNOLOGY**

**MASTER THESIS**

**Acoustic sensors for protein and cell binding**



**CHRONAKI DIMITRA**

**Pr. GIZELI ELECTRA**

**HERAKLION 2014**

## *GREETINGS*

There are many people who I would like to thank for the accomplishment of this study. First of all, I would like to thank my professor Dr. Electra Gizeli for giving me the chance to perform my master thesis at the biosensors laboratory. Except from the guidance and the continuous advising, my professor was really inspiring and allowed me to work on my own way. Moreover, I feel really lucky my professor urged me to attend the “Biosensors Meeting” on August 2013 and the “Soft-Inter” summer school on September 2014.

I would like to express my gratitude to Pr. Eirini Athanassaki and Pr. George Chalepakis for advising me regarding this thesis. Afterwards, I would like to thank my supervisor Dr. Achilles Tsortos who gave me a better understanding of Biophysics and Maths; he helped me also to interpret the results presented in this thesis. I really appreciate the fact that Dr. George Papadakis provided me his biological knowledge when needed and Dr. Dimitra Milioni taught me to analyze results using OriginPro8 software.

Also, I would like to thank Pr. George Zachos for allowing me to use cell culture facilities and Dr. Eleni Petsalaki who taught me cell culturing. I am grateful to Dr. Ema Anastasiadou who provided me with cell lines and the PhD student Vasiliki Taraslia for her help. Moreover, I thank my friend and co-worker MSc student Stratiotis Dimitris for allowing me use a part of his data in the thesis.

Special thanks to Antonis Kordas and Vaggelis Drougkas for their great friendship. Without the support of my family I wouldn't manage to fulfill my goals and finish master thesis. Finally, I thank Manos for taking care of me and constantly supporting me when I needed it.

## CONTENTS

<b>ΠΕΡΙΛΗΨΗ</b> .....	5
<b>ABSTRACT</b> .....	6
<b>CHAPTER1. INTRODUCTION</b>	
Protein adsorption on surfaces.....	7
Collagen.....	8
Fibronectin .....	9
Fibrinogen .....	10
Cell adhesion on surfaces.....	12
Thyroid cancer.....	14
Aim of the study.....	15
<b>CHAPTER2. MATERIALS AND METHODS</b>	
A) Preparation of protein solutions.....	16
1) Collagen.....	16
2) Fibronectin.....	16
3) Fibrinogen.....	16
B) Cell preparation and assays.....	17
1) Cell cultures.....	17
2) Cell stocks.....	17
3) Cell samples.....	18
C) QCM-D experiments.....	18
1) Protein adsorption experiments.....	18
2) Cell adhesion experiments.....	19
i. On Au surface.....	19
ii. On Fibrinogen-coated Au surface.....	19
3) RGD peptides.....	19
D) Optical microscopy.....	20
E) QCM-D data analysis.....	20

### CHAPTER3. RESULTS

#### Protein adsorption studies

- Collagen adsorption.....21
- Fibronectin adsorption.....24
- Fibrinogen adsorption.....26

#### Cell adhesion studies

- Cell substrate selection.....29
- Cell adhesion on fibrinogen-coated Au surface.....30
- Cell adhesion on Au surface.....33
- Cell adhesion on fibrinogen-coated Au surface.....35
- Kinetic analysis of QCM-D data.....38
- Optical microscopy images.....41
- RGD peptides.....43

### CHAPTER4. DISCUSSION AND CONCLUSION

- Discussion.....45
- Conclusion .....50

### CHAPTER5. REFERENCES

- References.....52
- Appendix
- Table A.....57
- Table B.....58
- Table C.....59
- Table D.....60

## ΠΕΡΙΛΗΨΗ

Στην παρούσα μελέτη, καταφέραμε να αποκτήσουμε καλύτερη εικόνα της πρόσδεσης πρωτεϊνών και κυττάρων σε επιφάνειες χρυσού με τη χρήση ακουστικού βιοαισθητήρα QCM-D με καταγραφή ενεργειακών απωλειών. Ειδικότερα, μελετήθηκε η προσρόφηση σε πραγματικό χρόνο τριών εξωκυττάρων πρωτεϊνών σε επιφάνειες χρυσού. Οι πρωτεΐνες που μελετήθηκαν ήταν το κολλαγόνο, η φμπρονεκτίνη και το ινωδογόνο και η προσρόφηση τους παρείχε σημαντικές πληροφορίες σε ότι αφορά τον προσανατολισμό τους πάνω στο χρυσό. Για την ερμηνεία των αποτελεσμάτων χρησιμοποιήθηκε το μοντέλο «Διακριτού Μορίου» το οποίο αποτελεί μια μοριακή προσέγγιση του στρώματος πρωτεϊνών σε αντίθεση με την κλασική προσέγγιση του πρωτεϊνικού στρώματος ως φιλμ. Η χρήση του ακουστικού λόγου (ενεργειακές απώλειες ανά μονάδα μάζας που προσδέεται στην επιφάνεια) σε συνδυασμό με την εξίσωση Sauerbrey που υπολογίζει την θεωρητική κάλυψη για μονοστιβάδα μορίων, κατάφερε να προβλέψει τον προσανατολισμό των μορίων πάνω στο χρυσό. Επιπλέον, πραγματοποιήθηκαν μελέτες κυτταρικής προσκόλλησης όπου χρησιμοποιήσαμε δυο κυτταρικές σειρές: υγιή (Nthy) και καρκινικά (ARO) ανθρώπινα κύτταρα θυρεοειδή αδένος. Ο ακουστικός αισθητήρας QCM-D επιστρατεύτηκε για την ανίχνευση και διάκριση δυναμικών «υπογραφών» μεταξύ των δύο κυτταρικών σειρών. Αλλαγές στη μάζα και ενέργεια του συστήματος καταγράφηκαν από τον αισθητήρα παράλληλα με εικόνες οπτικής μικροσκοπίας που απεικονίζουν την περιοχή όπου τα κύτταρα προσκολλήθηκαν. Η κατασκευή ισόθερμων καμπυλών πρόσδεσης απέδειξε ότι η διαδικασία κυτταρικής προσκόλλησης είναι άμεσα εξαρτημένη από την συγκέντρωση των κυττάρων που χρησιμοποιείται και ανέφερε διαφορετική ικανότητα προσκόλλησης πάνω στο υπόστρωμα μεταξύ των δυο σειρών. Τέλος, η κινητική ανάλυση των αποκτηθέντων σημάτων από τον αισθητήρα αποκάλυψε αξιοσημείωτες διαφορές των δυο σειρών πάνω στο υπόστρωμα.

## *ABSTRACT*

In this study we gained a better insight on protein adsorption and cell adhesion processes using the acoustic biosensor Quartz Crystal Microbalance with Dissipation monitoring (QCM-D). Specifically, real-time adsorption of three extracellular proteins was monitored on Au surfaces. The proteins tested were collagen, fibronectin and fibrinogen and their adsorption resulted in significant information regarding their orientation on Au. For results interpretation we used the “discrete model” theory, which is a molecular approach of the adsorbed layer rather than the usual film approach. Acoustic ratio measurements ( $\Delta D/\Delta F$ ) were combined with Sauerbrey equation for monolayer coverage to predict orientation of adsorbed molecules. Furthermore, cell adhesion studies were performed for two cell lines: normal (Nthy) and malignant (ARO) thyroid cells. QCM-D technique was recruited to distinguish dynamic cell adhesion signatures of the two cell lines. QCM-D frequency and dissipation shifts were accompanied by optical microscopy images of the adhered cells. Binding isotherms proved the concentration-dependent nature of cell adhesion process and report a different binding capacity of Nthy and ARO on Au. Finally, cell adhesion kinetics revealed remarkable differences of two cell lines on the underlying substrate.

## CHAPTER 1

### INTRODUCTION

---

Nowadays, scientists all around the world conduct multidisciplinary studies combining molecular biology with surface chemistry and biophysics. Acoustic sensor devices can track extremely small chemical, mechanical and electrical changes that take place on the sensing surface and convert them into measurable electrical signals [1]. An acoustic sensor system named Quartz Crystal Microbalance with dissipation (QCM-D) is able to monitor in real-time shifts in frequency ( $\Delta F$ ) and dissipation ( $\Delta D$ ) of the material coupled to the surface of the sensor crystal. QCM-D is a label-free and non-invasive technique. The merit of QCM-D lies in its high mass sensitivity (in the  $\text{ng}/\text{cm}^2$  range) and its simplicity. The above features of QCM-D constitute a powerful bioanalytical tool that has found many applications in protein adsorption and cell biology studies.

#### *Protein adsorption on surfaces*

Adsorption processes at the solid-liquid interface by which protein molecules bind on various surfaces, are of a great importance for biosensors, biomaterials and surface science. The understanding of the adsorption process and the three-dimensional organization (density, water content and thickness) of the resulting adsorbed film is crucial for many applications [2]. Moreover there is a need to monitor not only the amount of the dry adsorbed mass (sensitivity), but also changes in the viscoelastic properties (viscosity and shear modulus) of the film and the contribution of the solvent molecules to the film formation. QCM-D can provide us with reliable qualitative curves for protein adsorption; the extraction of quantitative physical parameters (optical index, density, viscosity, water content) requires modeling of the adsorbed layer. More information for adsorbed layers can be gained by the combination of acoustic and optical biosensors with Ellipsometry optical technique and Atomic Force Microscopy imaging (AFM).

In general, protein adsorption involves a fast early step with monolayer adsorption where molecules adopt an almost flat orientation, followed by slower conformational and orientational rearrangements of these molecules. These conformational changes that occur during protein adsorption on solid surfaces can determine the adsorption mechanism. Protein adsorption is affected by many factors as: electrostatic interactions, surface charge, ionic strength, isoelectric point (of the surface and protein), hydrophobic interactions, intra- and intermolecular protein interactions and temperature. Additionally, surface physical features such as roughness, rheology and morphology may affect protein adsorption.

## Collagen

Type I collagen is a fibrillar protein of the extracellular matrix; the molecule contains a right-handed triple helix with dimensions about 300nm in length, 1.5nm in diameter and a molecular weight of 300kDa (Fig.1). Each polypeptide chain is a left-handed helix that consists of a repeating aminoacid sequence  $(G-X-Y)_n$ , where glycine (G) is found every third residue and about 20% of X-Y positions are occupied by proline and hydroxyproline [7, 8]. Collagen is an extremely slender structural protein with relatively high stiffness because of its triple helical structure [3]. Collagen intrinsically possesses self-assembly properties [8] and forms fibrils in vivo as well as in vitro. Collagen molecules are able to preserve the morphology of tissues in a physiological environment, by aggregation and crosslinking in order to form mechanically stronger bundles [4].

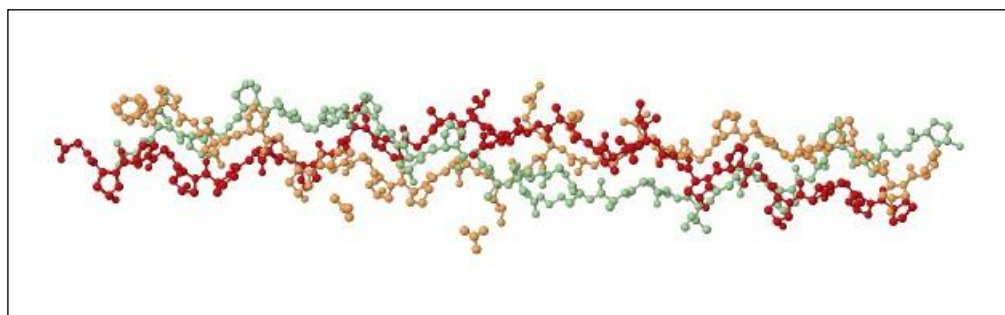


**Figure1.** Three dimensional structure of Human collagen (PDB ID: 1BKV) viewed in Jmol. Ball and stick model is used and each polypeptide chain has a distinct color.

Up to date, collagen has been used in many adsorption studies. Spatial organization and adsorption kinetics of collagen films on polymer substrates (PS: polystyrene and PSox: plasma-oxidized polystyrene) with a different degree of hydrophobicity, were investigated by QCM-D, AFM and radioassays [5]. Also, the effect of heat denaturation on the nanoscale organization and mechanical properties of collagen layers on polystyrene substrate was identified by QCM-D, AFM and X-ray photoelectron spectroscopy (XPS) [6]. The stabilization of collagen molecules treated with different crosslinking agents was studied by surface rheology and QCM-D [9]. Additionally, a study compared the adsorption profile of lysozyme (spherical shape) with collagen (fibrous shape) on gold surfaces using QCM-D and investigated the impact on adsorption of the conformation and aggregation of collagen by Circular Dichroism (CD) measurements [3].

The fact that collagen assemblies provide a major biomechanical scaffold for cell attachment and anchorage of macromolecules [8] has established collagen as the most common substrate for cell biology studies [10-14]. Specifically, fibroblasts were

seeded in-situ on collagen-coated SiO<sub>2</sub> crystals and their attachment was monitored in real-time by QCM-D and light microscopy [10]. Also, a promising experiment was the use of collagen-conjugated supported lipid bilayer as a culture platform for smooth muscle cells [12]. Finally, collagen self-assembled layers coating titanium surfaces served as a good substrate for osteoblast proliferation and differentiation [11].

### *Fibronectin*

Fibronectin is a well-characterized extracellular matrix protein present in body fluid and connective tissue. It is a high-molecular-weight (450kDa) dimeric glycoprotein [16]. Fibronectin consists of two nearly identical monomers (60nm in length and 2.5nm in diameter) connected by flexible disulfide bonds [15]. Each monomer contains three types of modules: type I, II and III. All three modules are composed of two anti-parallel  $\beta$ -sheets; however type I and type II are stabilized by intra-chain disulfide bonds, while type III modules do not contain any disulfide bonds (Fig2). Fibronectin exists in two forms: as an extracellular matrix protein and as a plasma protein. The ECM form is an insoluble glycoprotein dimer which links the protein with the ECM and is synthesized by fibroblasts, chondrocytes, endothelial cells, macrophages and certain epithelial cells. The plasma form is a soluble disulfide-linked dimer found in the plasma and synthesized by hepatocytes [16]. Fibronectin in cooperation with other proteins like vitronectin, fibrinogen, collagen, laminin and osteopontin, can mediate specific cell-surface interactions via cellular integrin receptors [17]. Thus, fibronectin plays a major role in the adhesion, migration and differentiation of cells, and also participates in wound healing and embryonic development processes.

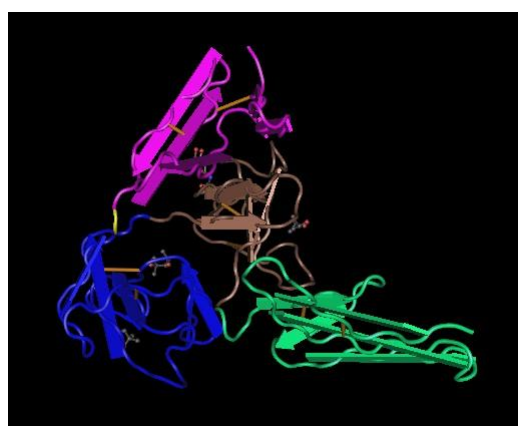


**Figure2.** Crystallographic structure of human fibronectin fragment (PDB ID: 3MQL) viewed in Cn3D. Each domain has a distinct color.

Fibronectin adsorption on various surfaces has been extensively studied in the past with many techniques [15, 16, 18-25]. Firstly, the amount, density and structural

orientation of the adsorbed fibronectin layer on silicon oxide (SiO<sub>2</sub>) surfaces have been examined using Neutron Reflectometry (NR) in conjunction with QCM-D technique [15]. Then, the interactions of fibronectin with thin polymer films were studied in displacement experiments using Human Serum Albumin (HSA) and analyzed by QCM and Confocal Laser Scanning microscopy [18]. In addition, the conformation and orientation of a fibronectin layer formed on gold, Ti-oxide and Ta-oxide surfaces under physiological conditions, were investigated using QCM-D technique and random sequential adsorption (RSA) model [19]. Also, adsorption of fibronectin on hydroxyapatite (HA) and gold surfaces was examined by QCM-D technique and Atomic Force Microscopy (AFM), with respect to the amount of fibronectin bound on these surfaces and the activity of individual fibronectin molecules upon adsorption [20]. In another study, Optical Waveguide Lightmode Spectroscopy (OWLS) and QCM-D techniques were employed to characterize the assembly of fibronectin-terminated multilayer films composed of the linear polyelectrolytes poly(L-lysine) (PLL) and dextran sulfate (DS) [24]. Finally, competition of three proteins (bovine serum albumin, fibrinogen and fibronectin) adsorbed on TiO<sub>2</sub> surface was monitored by QCM-D and the properties of the adlayer were calculated by the Voigt model [25].

Fibronectin molecule has been extensively used a substrate for cell adhesion studies [10, 26-37]. The adhesion of NIH3T3 fibroblasts to albumin and fibronectin precoated tantalum (Ta) and oxidized polystyrene (PSox) surfaces was examined using the QCM-D monitoring and fluorescent microscopy, confirming the importance of the underlying substrate for matrix remodeling of cells [26]. Moreover, functionalization of oxidized polystyrene (PSox) and SLB (Supported Lipid Bilayer) coated silicon oxide with ECM proteins (fibronectin, collagen, BSA) served as a platform for cell adhesion of NIH3T3 fibroblasts; QCM-D, immunofluorescent staining and microscopic imaging were utilized to characterize the system [27].

### ***Fibrinogen***

Fibrinogen is a fibrous glycoprotein composed of pairs of three non-identical polypeptide chains ( $\alpha_2\beta_2\gamma_2$ ); it is present in the blood plasma of all vertebrates. Human fibrinogen is an extracellular protein with a size of (45 x 9 x 6) nm<sup>3</sup> and a molecular weight of 340kDa (Fig.3). Fibrinogen plays an important role in blood coagulation cascade; fibrinogen adsorbs on the edges of tissue damage where it is converted by thrombin protease into fibrin. Then individual fibrin monomers polymerize to form an insoluble fibrin clot. Briefly, in order to form fibrin thrombin removes small peptides from the NH<sub>2</sub>-term of  $\alpha$  and  $\beta$  chains, thus exposing sets of “knobs” that interact non-covalently with “holes” lying on neighboring molecules to

form oligomers (proto-fibrils). As polymerization goes on, factor XIII -activated by thrombin- incorporates covalent cross-links between the C-term parts of  $\gamma$ -chains and finally  $\alpha$ -chains too. Afterwards, proto-fibrils somehow associate to form the macroscopic fibers of the clot [38].

Fibrinogen is found in blood in concentrations of about 3mg/ml and the understanding of fibrinogen adsorption on metal surfaces is really important, as fibrinogen layers formed at liquid-solid implant interface may trigger an inflammatory response and lead to acceptance or rejection of implant [39].

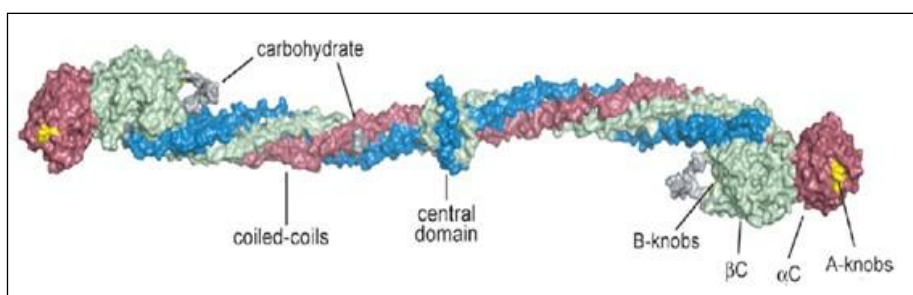


**Figure3.** Space-filling model of Human fibrinogen molecule (PDB ID: 3GHG):  $\alpha$ -chains (green),  $\beta$ -chains (blue) and  $\gamma$ -chains (red) [38].

It is notable that fibrinogen is a “sticky” protein able to adsorb well on many biocompatible surfaces. This is the reason why many adsorption studies used fibrinogen as a surface-functionalizing substrate [25, 39-45]. To begin with, adsorption of human fibrinogen on tantalum oxide, titanium oxide and gold surfaces under physiological conditions (pH 7.4, 37°C) was studied by QCM-D technique [39]. Kinetic data of fibrinogen adsorption on a gold surface were acquired by QCM-D and conformational changes of the adsorbed layer were revealed by Enzyme-Linked Immunosorbent Assay (ELISA) [40]. A really innovative study coupled QCM-D with MALDI-ToF mass spectrometry; Human Serum Albumin, Fibrinogen, Fibronectin adsorbed on SAM-coated (Self-Assembled Monolayer) sensor devices and a subsequent on-chip digestion unraveled the composition of the adsorbed protein layer [41]. Two different studies employ the same techniques (QCM-D, XPS and AFM) to explore different system properties: the one tries to understand the mechanism of protein-protein resistance through adsorption experiments on soy protein films [42], while the other creates a protein resistant self-assembled monolayer by a selective oxidization step [43].

As fibrinogen is a main plasma component, it is utilized for blood coagulation [46, 47] and hemocompatibility research [48, 49]. Yao C. (2013) used QCM method to detect the concentrations of fibrinogen and coagulation factor VIII in clinical plasma

samples and then compared the QCM results with the results acquired by a common clinical technique termed Optical Coagulometer (OC) [46]. Also, QCM monitored the adsorption of fibrinogen on four different surfaces along with the subsequent fibrin proliferation, in combination with Scanning Electron Microscopy which characterized the polymerized film morphology [47]. Furthermore, QCM gold sensors were coated with hemocompatible films and fibrinogen to assess cell resistance and possible applications of this film for blood contacting sensors [48]. Similarly, the organization of fibrinogen molecules at the material interface of blood contacting devices was evaluated to be crucial for bioengineering successful interactions with endothelial cells (HUVEC), followed by neovascularization and final acceptance of the implant [49].

### *Cell adhesion on surfaces*

Cell adhesion phenomenon has been of a great interest because it plays important roles in the regulation of cell behavior, especially for processes as growth, differentiation, migration and survival of cells. Cell adhesion process incorporates multiple complex events: the specific binding of membrane proteins with ECM, the formation of intracellular cytoskeleton and the signal transduction pathway. The strictly controlled cell adhesion process is driven by ligand-receptor interactions, mostly by integrin binding [50]. Integrin transmembrane receptors can recognize ECM ligands, such as fibronectin, collagen, vitronectin and laminin. Integrin binding transfers signals from the ECM in the cytoplasm of the cell. Upon binding, intracellular cytoskeleton (actin, microtubules and intermediate filaments) reforms and new actin filaments form thus determining cell shape and structure. Actin filament network is intrinsically connected to ECM proteins through integrin receptors. Cell adhesion is a dynamic process where cells can modify cell-ECM interactions and extracellular signaling by rearranging fibrillar elements, reorganizing ECM or secreting new proteins [51].

Most integrins recognize the tripeptide arginine-glycine-aspartic acid (RGD) sequence in many extracellular proteins [52]. RGD motif serves as a shared binding site while a second binding site on the protein generates specificity. The anti-adhesive properties of RGD peptides have been used by many cell adhesion studies, in order to compete with the binding of ECM proteins to integrin receptors. For example, Wegener used RGDs to inhibit the integrin-mediated attachment and spreading of mammalian cells and demonstrated that this inhibition depends on the peptide concentration and aminoacid sequence [53]. Li et al. [34] independently stated that the inhibition of mammalian cell adhesion is dependent on the specific

aminoacid sequence of RGD peptide. Also, pretreatment of endothelial cells with soluble RGD could significantly retard the rate of initial cell adhesion [54].

As stated before, cell-substrate adhesion requires the synchronization of many molecular events inside and outside of the cell. In the cell-substrate adhesion procedure (Fig.4) cells contact the surface, loosely attach to it, flatten and spread their membrane on the underlying substrate [55]. There, adhesion complexes are formed by cells to connect ECM with intracellular actin filaments (stress fibers) through integrin receptors. These complexes establish focal adhesion (FAs) of cells which anchor cells on the substrate-coated surface. In the periphery of the cell body the thin sheet-like lamellipodia and spike-like filopodia are frequently observed. These structures reorganize continuously to maintain the cell shape and copy with the external stimuli.

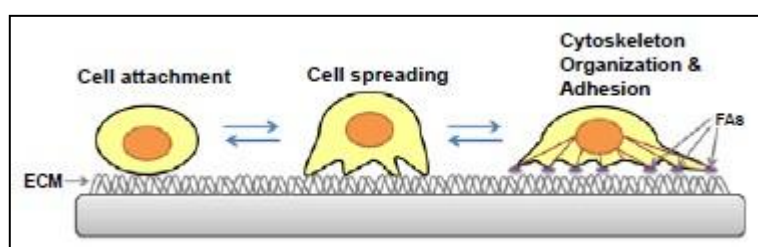


**Figure4.** Cell adhesion process includes the creation of adhesion complexes and focal adhesion points [55].

QCM sensors have been broadly used for the study of eukaryotic cell adhesion. Sensors can in real-time detect mass adsorption in liquid and differences in viscoelastic properties of the adsorbed biological layer and provide further information for cell behavior. Until now, many cell lines have been studied for various concentrations, different protein substrates and sensor devices. The results report that there is a linear relationship between the surface coverage with cells and the frequency shift of the quartz crystal. When the surface is fully covered with cells (plateau) there is no additional signal change.

For cell adhesion experiments, the Sauerbrey equation [56], which correlates changes in the oscillation frequency of a piezoelectric crystal with the mass deposited on it, is not valid. This happens because a) the cells have viscoelastic properties and b) the lateral sensitivity varies over the QCM surface as cells spatially distribute on it [57]. The viscoelasticity of cells produces energy losses on the oscillating crystal and contributes to the dissipation factor. Energy dissipation is believed to arise from properties in the liquid trapped in the cell-surface interface, in the cell membrane and in the interior of cells [58]. Also, Wegener et al. [59] proposed that dissipation shifts are related to extracellular matrix changes, actin cytoskeleton and details in the cell-substrate interface.

It is notable when studying a cell layer from the QCM-D theory and modeling point of view, that it constitutes a complex entity with heterogeneity parallel and perpendicular to the sensor surface and that the sensing depth is much smaller than the cell thickness [10]. So, unlike thin rigid films (which follow Sauerbrey equation) where frequency shifts are proportional to the adsorbed mass, cell signals require more advanced modeling and combination of QCM with other techniques. Additional information for cell adhesion process can be gained from D-f plots which characterize the effective deposited mass, its viscoelastic properties, the structure and shape of cells and how adhesion process evolves in time, thus providing unique **fingerprints** for each cell type [60].

Briefly, Hayes et al. [61] summarize the influence of surface properties on the response of cells when meeting the surface. The factors involved in the surface-dependent cellular response (especially for implants) are a) surface chemistry, b) surface topography, c) surface roughness and d) mechanotransduction (for signal propagation).

### *Thyroid cancer*

Thyroid carcinomas constitute the 1-2% of all malignant tumors and represent the most common tumors of the endocrine system, after those of the gonads. The thyroid tumors include several histotypes with different molecular, biological and clinical behaviors. There are two well-investigated histotypes: papillary (PTC) and anaplastic (ATC) thyroid carcinomas [62]. Firstly, PTC represents the 80% of all thyroid tumors; it is well differentiated, with high occurrence and a good prognosis. ATC comprises less than 5% of thyroid tumors and represents one of the most deadly and aggressive human malignancy. Because ATC is rare, it has been difficult to examine an adequate number of patients to gain a better clinical image of the disease and understanding of the natural history of the tumor [63].

Up to date, therapy of ATC includes surgery, chemotherapy and radiation therapy, which can expand the patients' life for 3 years, for those who can tolerate these aggressive therapies [64]. Additionally, fine needle aspiration (FNA) is the most common technique used to obtain samples of thyroid tissue cells for further diagnostic evaluations [65]. The results from FNA are often inconclusive and it is difficult to distinguish between benign and malignant neoplasms. As a matter of fact, patients with ambiguous FNA biopsy results are often subjected to diagnostic hemithyroidectomy. For the 80% of these patients the surgery proved to be unnecessary.

The biological mechanism of thyroid tumorigenesis is still unclear. Several studies of gene expression profiling and immunohistochemistry for thyroid tissue and cell lines have been conducted in order to identify putative diagnostic biomarkers for thyroid cancer. Gene expression studies have compared cancer with non-cancer thyroid cells and identified a cluster of up-regulated genes including MET, SERPINA, FN1, CD44 and DPP4, while other genes found to be down-regulated (including TFF3) [65]. Recently, researchers exploit the powerful proteomic technology to find biomarkers indicative of thyroid malignancy [62, 65]. Based on the above, there is a need to establish more specific methods to distinguish cancer from healthy cells and to develop better approaches to discriminate various types of thyroid cancer.

### *AIM OF THE STUDY*

---

In the first part of this study QCM-D technology is recruited to monitor in real-time the adsorption of extracellular proteins collagen, fibronectin and fibrinogen on gold crystals. Application of the acoustic ratio  $\Delta D/\Delta F$  as a means to study adsorption processes and characterize the conformational and orientational changes that protein molecules undergo, is reported.

In the second part, QCM-D sensor technology is utilized to identify cell-substrate interactions and their kinetics, as a way to understand dynamic cell adhesion processes. Specifically, attention was paid to the differentiation of normal follicular cells (Nthy.ori 3-1) from ATC (ARO) ones, based on their binding capacity and kinetics on ECM proteins. Complementary light microscopy images are cited in order to compare the shape and morphology of adhered cells (tumor and healthy) on their underlying substrate.

## CHAPTER 2

### MATERIALS AND METHODS

---

#### A) Preparation of protein solutions

##### 1) Collagen

Type I collagen from calf skin (Sigma-Aldrich, Product number: C3511) (MW: 300kDa) was dissolved in a cold acetic buffer (4°C) that was filtered through 0.22µm diameter filters (Millex) prior to use. This buffer consists of distilled water and acetic acid (CH<sub>3</sub>COOH) with final pH≈3.0. In order to dissolve collagen in acetic buffer, dialysis of the protein sample occurs at 4°C overnight under shaking to give 0.1mg/mL stock solutions. Stock solutions were stored at 4°C until use. Collagen solution concentration was estimated via NanoDrop spectrophotometer (Thermo Scientific, ND-1000). Triplicates of collagen stock dilutions were measured by NanoDrop and an average concentration was calculated for the whole stock. For QCM-D experiments fresh dilutions of collagen in PBS buffer were prepared at working concentrations of 0.5, 1, 5, 10, 40 and 100 (µg/mL).

##### 2) Fibronectin

Fibronectin from bovine plasma (Sigma-Aldrich, Product number: F4759) with an approximate molecular weight of 450kDa, was dissolved in sterile distilled water at 1mg/mL and dialyzed for 30 minutes at 37°C. When fully reconstituted, fibronectin solution was stored in aliquots at -20°C until use. Fresh dilutions of fibronectin were prepared for each QCM-D experiment in PBS buffer solution at working concentrations of 10, 20, 40 and 50 (µg/mL).

##### 3) Fibrinogen

Fibrinogen from bovine plasma (Merck Millipore, Cat. number: 341573), with a molecular weight of 330kDa, contains more than 95% clottable proteins and is homogeneous by SDS-PAGE. Fibrinogen was dissolved in sterile distilled water (preheated at 37°C) at about 2mg/mL concentration and solubilized in a 37°C waterbath for 1hr. Reconstitution of fibrinogen is a slow process that can be accelerated by pipetting of the sample. After reconstitution, protein aggregates were removed by centrifugation (15.000rpm, 5min, RT) and final protein stocks were stored at 4-8°C. In order to estimate fibrinogen concentration, dilutions of the stock were measured in triplicates via NanoDrop spectrophotometer. Before QCM-D experiments, fresh dilutions of fibrinogen were prepared in PBS with final concentration: 10, 40 and 100 (µg/mL).

## **B) Cell preparation and assays**

### **1. Cell cultures**

Two thyroid cell lines, Nthy.ori 3-1 (Normal human primary thyroid follicular epithelial cells) and ARO (poorly differentiated anaplastic carcinoma) were kindly provided by E. Anastasiadou (Biomedical Research Foundation Academy of Athens). These cells are grown with RPMI 1640 medium (Lab supplies, LM-R1641/500) supplemented with 10% v/v Fetal Bovine serum (Biowest, S1810-500) (inactivated at 56°C for 30min), 2mM L-glutamine (Lab supplies, XC-T1715/100) and 1% v/v penicillin-streptomycin (Lab supplies, XC-A4122/100). The cells were grown in tissue culture plates (100x20(mm), BD Falcon) in a 37°C humidity-controlled incubator with 5%CO<sub>2</sub>.

As these cell lines have to adhere to the tissue culture plate surface to proliferate, they give a surface coverage that depends on their growth rate. Every 2-3 days cells reached an 80-90% surface coverage so that culture medium had to be replaced and cells to be diluted by a process called "Split". In this process, old medium is discarded and cells are washed twice with sterile PBS. Then, 1mL of 1X trypsin-EDTA solution (Lab supplies, LM-T1706/100) is added and culture plate is placed for 5min inside the incubator. Cells detach from the plate and are collected with 5mL of RPMI 1640 full medium. Cell pellet is collected by centrifugation (1.200rpm, 5min, RT) and only an appropriate dilution of cells is added in the culture plate with 10-15mL of RPMI. Then, the culture plate is returned to the incubator.

### **2. Cell stocks**

Starting cell cultures begin with the transfer of a stock cryovial from -80°C to ice. As soon as cells thaw, are reconstituted with 5mL RPMI 1640 full medium and centrifuged (1200rpm, 5min, RT). Supernatant is discarded; cell pellet is reconstituted with 7mL RPMI 1640 full medium and placed to a culture plate (60x15(mm), Nunc) at 37°C incubator. The day after, dead cells are removed and healthy cells are transferred to a bigger culture plate (100x20(mm), BD Falcon) at 37°C incubator. In this way, following cell cultures will contain only cells that managed to recover from the thawing process.

After a week of the starting cell cultures, when cells remained healthy, the stock preparation took place. In order to create cell stocks the surface of the tissue culture plate had to be saturated with cells (surface coverage >90%). Cells were washed twice with sterile PBS solution and detached from the culture plate with trypsin-EDTA. Afterwards, they were collected with RPMI 1640 full medium and centrifuged (1200rpm, 5min, RT). Cell pellet was reconstituted with a mixture of 10% DMSO (Roth) and 90% FBS without frothing of the suspension. Cell suspension (0.9-1mL

volume) was quickly transferred into cryovials (Thermo Scientific) and then placed into a cryo-1°C-freezing container (Cat.No. 5100-001) at -80°C. The next day, the cryo-freezing container is removed and cell stocks remain at -80°C.

### **3. Cell samples**

For QCM-D experiments cells were washed twice with sterile PBS and removed from culture plates by trypsin-EDTA solution. The trypsin-cell suspension was centrifuged (1.200rpm, 5min, RT) and then a subsequent washing step with 5mL PBS was used to remove serum proteins. The pellet was resuspended in 5mL PBS and the number of cells was calculated via trypan blue (Biosera, LM-T1708/100) on a Neubauer slide, using an inverted light microscope (Zeiss HAL 100). Trypan blue exclusion assay proved that dead cells never exceeded 5% of total cells. When the approximate number of cells per mL of suspension was determined, dilutions of cells in PBS were made with a final volume of 0.5mL. Various concentrations ( $1 \cdot 10^4$ - $2 \cdot 10^5$  cells/mL) of cells prepared were left in RT until the QCM-D experiment.

### **C) QCM-D experiments**

The QCM-D technique is based on a quartz crystal sandwiched between two gold electrodes. The quartz crystal is driven by applying an alternating electric field at its resonance frequency of 5 MHz or at one of its first three overtones: 15, 25, or 35 MHz. When electric field is applied on the crystal a lateral oscillation starts. The equipment measures very small masses added on the sensor surface because an increase in mass ( $\Delta m$ ) bound to the quartz surface causes the crystal oscillation frequency to decrease, obtaining a negative shift of the resonant frequency ( $\Delta f$ ).

The QCM-D experiments were performed using a Q-sense E4 (Biolin Scientific) instrument and AT-cut quartz disks (with fundamental frequency 5MHz). Gold coated quartz sensors were rinsed with 100% acetone solution, distilled water and then dried with Nitrogen ( $N_2$ ). Gold crystals were then cleaned and sterilized with air plasma (600 mTorr). Gold crystals were placed inside the measuring chambers prior to the beginning of QCM-D experiments. All QCM-D experiments were performed under flow conditions.

#### **1) Protein adsorption experiments**

The adsorption experiments were performed at 37°C with a constant flow rate (50 $\mu$ L/min for fibronectin and 30 $\mu$ L/min for collagen adsorption). Fibrinogen adsorption experiments were conducted at 25°C with a flow rate of 50 $\mu$ L/min. The crystal was equilibrated with PBS (Sigma-Aldrich, Product number: P4417) before the addition of collagen, fibronectin and fibrinogen. Finally, the adsorbed proteins were

rinsed with PBS. The adsorption of these proteins on gold surface can be described by the frequency and dissipation shifts as monitored by the Q-sense instrument.

## **2) Cell adhesion experiments**

### **i. On Au surface**

These control experiments are performed at 25°C with a constant flow rate of 10µL/min. Gold sensors were equilibrated with PBS and then various concentrations of Nthy or ARO cells were injected in the measuring chamber, until plateau was achieved. Thence, PBS rinse removed unbound cells and stabilized the frequency and dissipation signal.

### **ii. On Fibrinogen-coated Au surface**

The temperature used for this set of experiments is 25°C. Initially, PBS buffer equilibrated the sensor crystal (50µL/min). The first step of these experiments included the adsorption of 10µg/mL of fibrinogen solution. When fibrinogen fully covered the crystal, a PBS rinse followed and the flow rate was set at 10µL/min prior to the addition of cells. In the second step, Nthy or ARO cell dilutions were continuously inserted in the system until a pseudo-plateau was achieved. The cell adhesion experiment was completed with a PBS buffer rinse.

The above cell adhesion experiment was repeated with slightly different conditions at 25°C. The first step is the same with fibrinogen molecules saturating the gold crystal (flow rate: 50µL/min), while the following PBS rinse is adjusted at a 30µL/min flow rate. Then, four volumes (0.5mL) of cell dilutions are added and rinsed with PBS. This experiment is shorter than the aforementioned experiment.

## **3) RGD peptides**

RGD peptides (Sigma-Aldrich, A8052) with a molecular weight of 346.3 Da, were dissolved in 0.1N acetic acid buffer at a final concentration 20mg/mL. The stock solution was stored at -20°C until use. Dilutions of stock were prepared in PBS prior to QCM experiment, at working concentrations of 0.1 and 0.3mg/mL.

- i.** Excess of RGD peptides (0.3mg/mL) was inserted in a fibrinogen-coated gold crystal (as described at section C1) with a flow rate 10µL/min and rinsed with PBS.
- ii.** Before the cell adhesion experiment (C2ii), Nthy cell samples ( $2 \cdot 10^4$  cells/mL) were incubated with 0.1mg/mL of RGD peptide for more than 90 minutes period of time. Then, Nthy-RGD cells were inserted into the fibrinogen-coated crystal in parallel with Nthy cells without RGD and rinsed with PBS.

- iii. At the end of the cell adhesion experiment (C2ii) of ARO cells ( $2 \times 10^4$  cells/mL), 0.1mg/mL of RGD peptides was inserted with a flow rate of 10 $\mu$ L/min and rinsed with PBS.

#### ***D) Optical microscopy***

At the end of a cell adhesion experiment, gold crystal was removed from the measuring chamber of Q-Sense instrument. Gold crystal was gently put on a microscope slide. Then a glass coverslip (usually 15mm diameter) was placed on the sensing side of the crystal, to keep the sample hydrated. The crystal was observed by Nikon Eclipse E800 light microscope and images of the biological sample were taken by ProgRes microscope camera (Jenoptik).

Artificial QCM devices were manufactured and kindly provided by T. Kostopoulos (Microelectronics Department, University of Crete). Glass coverslips (VWR, Cat.No. 631-0149) with diameter 13mm and thickness 0.14mm were cleaned with acetone, propanol and water (of high resistance). Then, coverslips were inserted in a vacuum chamber ( $10^{-7}$  Torr) of an Electron Beam Evaporator (Temescal BJD-1800). Briefly, electrons emitted accelerate inside an electric field ( $\sim 10$  kV) to acquire high energy and their direction is controlled by a magnetic field. Finally, the electron beam meets the metal goal. Then, evaporated metal atoms deposit on the glass substrate. This evaporation method was used to cover glass coverslips with Cr (15nm thickness) and then Au (15nm thickness), resulting in a new surface that resembles the surface properties of commercially available QCM crystals. These artificial devices were placed inside the measuring chamber of Q-Sense. Cell adhesion experiments (C2ii) were performed on these devices without monitoring  $\Delta F$  and  $\Delta D$  signals simultaneously with at least one control experiment on a gold QCM crystal (with dissipation and frequency monitoring). At the end of the experiment, artificial devices were covered with glass coverslips (diameter 15mm) and observed via Nikon Eclipse E800 light microscope.

#### ***E) QCM-D data analysis***

QCM results were processed with OriginPro8 software to perform data analysis, statistics and graphs. Additional mathematical and curve fitting analysis was provided by the software. Also, optical microscopy images were processed by Adobe Photoshop C5.

### Protein Adsorption Studies

Adsorbed mass of thin and nondissipative layers can be calculated using the Sauerbrey relationship (1):

$$\Delta m = -\frac{C}{n} \Delta f n \quad (1)$$

where  $\Delta f$  is linearly related to the adsorbed mass,  $C$  is the mass sensitivity constant ( $C = 17.7 \text{ ng cm}^{-2} \text{ Hz}^{-1}$  at 5MHz) and  $n$  is the overtone number ( $n = 1, 3, 5, 7..$ ). However, Sauerbrey equation cannot be applied for hydrated and highly viscous surface adsorbed protein layers that result in high dissipation shifts. In order to calculate the adsorbed mass and viscoelastic properties of such layers, more advanced theoretical modeling of QCM-D response is required in view of the "Voigt model". In this model the adsorbed layer is represented by four parameters: effective density ( $\rho$ ), shear viscosity ( $\eta$ ), thickness ( $\delta$ ) and shear elastic modulus ( $\mu$ ). An alternative way to express acoustic measurements is plotting dissipation versus frequency, a term called acoustic ratio  $\Delta D/\Delta F$ . This ratio represents the energy loss per unit of attached mass and provides qualitative and quantitative information on the intrinsic properties and morphology of the sensed surface. Indeed, acoustic ratio depends on the deposited mass, its viscoelastic properties, the shape and structure of the adsorbed molecules and how these parameters evolve in time [60, 66-68].

For further interpretation of our results, the Sauerbrey equation (1) can be modified by introducing features as the molecular weight and molecular dimensions of each protein, resulting in the equation:

$$\text{Monolayer coverage (Hz)} = \frac{MW(\text{Da})}{15.2(axb)(\text{nm}^2)} \quad (2)$$

This equation (2) can calculate the monolayer coverage (Hz) for a protein layer with molecules of given molecular weight (Da) and molecular dimensions ( $axb$ ), where  $axb$  ( $\text{nm}^2$ ) is the specific footprint of each molecule adsorbed on the surface.

#### ➤ Collagen Adsorption

Collagen adsorption studies on gold surfaces were conducted at comparable conditions and for various collagen concentrations: 5, 10 and 40 ( $\mu\text{g/mL}$ ). Real-time graphs and D-f plots are given below (Fig.5) and average values are calculated (Table1).

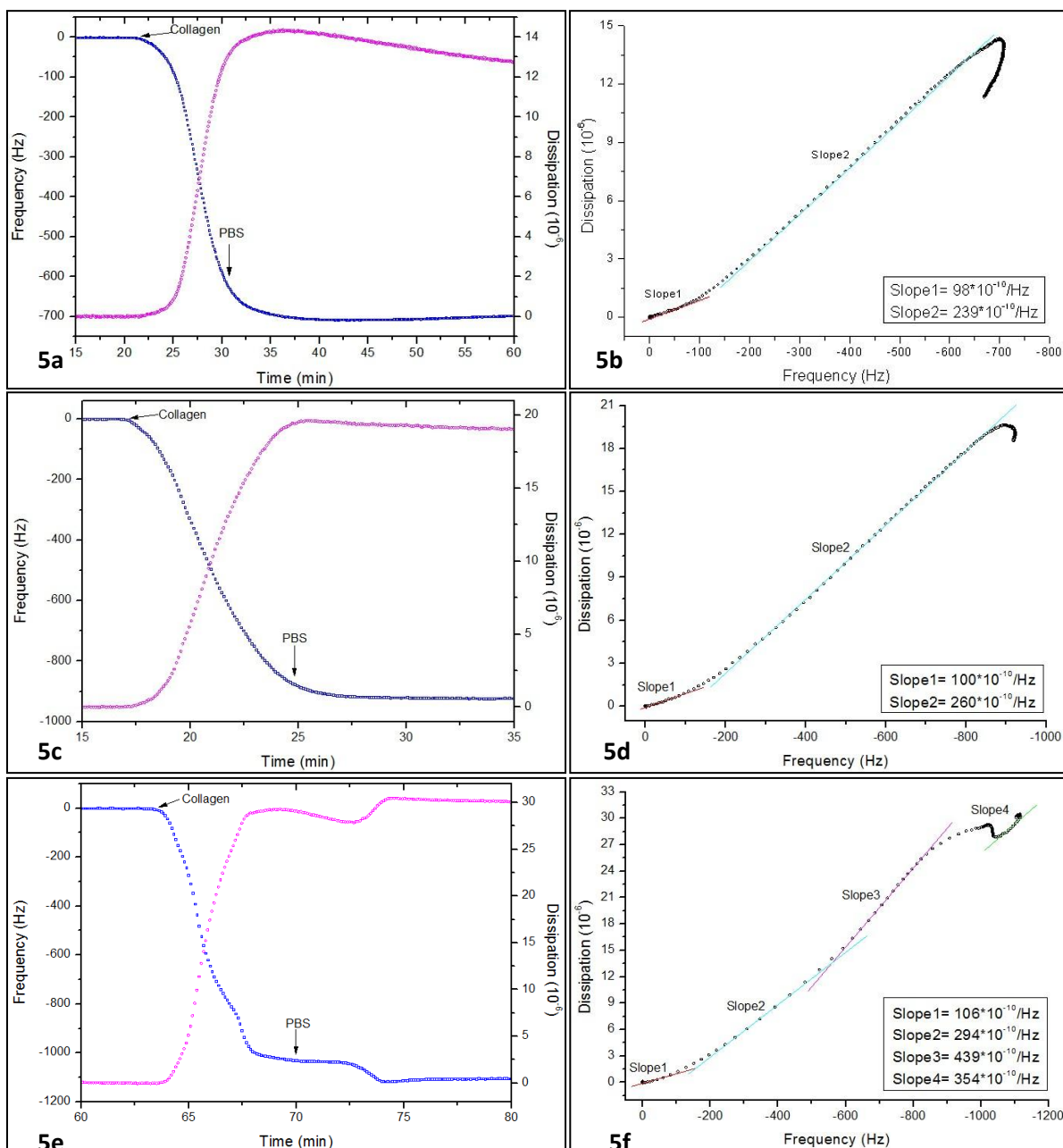


**Figure 5.** Collagen adsorption real-time graphs (a, c, e) and D-f plots (b, d, f). Specifically, graphs depict adsorption of 5µg/mL (a and b), 10µg/mL (c and d) and 40µg/mL (e and f) of collagen on gold sensors.

Collagen concentration	$\Delta F$ (Hz)	$\Delta D$ ( $10^{-6}$ )	Slope1 ( $10^{-10}/\text{Hz}$ )	Slope2 ( $10^{-10}/\text{Hz}$ )	Slope3 ( $10^{-10}/\text{Hz}$ )	Slope4 ( $10^{-10}/\text{Hz}$ )	Number of experiments
5µg/mL	763±139	17±7	103±11	259±41	-	-	3
10µg/mL	916±199	23.5±9	116±26	292±48	-	-	3
40µg/mL	1088±23	28.9±1.4	102±14	293±2.5	447±9	257±84	3

**Table 1.** Average values of  $\Delta F$ ,  $\Delta D$  shifts and slopes of individual collagen adsorption experiments, compared for same experimental conditions.

Real-time graphs (Fig.5a, c and e) of collagen adsorption depict frequency and dissipation shifts as a function of time;  $\Delta F$  and  $\Delta D$  shifts are represented with blue and magenta color respectively. Three concentrations of collagen are tested here. For concentrations 5  $\mu\text{g/mL}$  (Fig.5b) and 10 $\mu\text{g/mL}$  (Fig.5d), collagen adsorption process can be described by two slopes. For 5 $\mu\text{g/mL}$  acoustic ratios are  $\Delta D/\Delta F=103\pm 11$  ( $10^{-10}/\text{Hz}$ ) (slope1) and  $\Delta D/\Delta F=259\pm 41$  ( $10^{-10}/\text{Hz}$ ) (slope2). Similarly, for 10  $\mu\text{g/mL}$  acoustic ratios are  $\Delta D/\Delta F=116\pm 26$  ( $10^{-10}/\text{Hz}$ ) (slope1) and  $\Delta D/\Delta F=292\pm 48$  ( $10^{-10}/\text{Hz}$ ) (slope2). For higher collagen concentrations, adsorption process is described by at least three slopes (Fig.5f). Specifically, 40 $\mu\text{g/mL}$  result in acoustic ratios with values:  $\Delta D/\Delta F= 102\pm 14$  ( $10^{-10}/\text{Hz}$ ) (slope1),  $\Delta D/\Delta F= 293\pm 2.5$  ( $10^{-10}/\text{Hz}$ ) (slope2) and  $\Delta D/\Delta F= 447\pm 9$  ( $10^{-10}/\text{Hz}$ ) (slope3). Also, an additional slope is calculated here:  $\Delta D/\Delta F= 257\pm 84$  ( $10^{-10}/\text{Hz}$ ) (slope4). One can easily observe (Table1) that for the three different collagen concentrations and for close  $\Delta F$  shifts, the first two slopes have similar values.

Collagen molecular dimensions are (300x1.5)  $\text{nm}^2$  and its molecular weight counts for 300kDa. The two possible orientations of adsorbed collagen on gold surface are the “flat-on” and the “standing” mode (Fig.6). For the “flat-on” mode collagen’s footprint is (300x1.5)  $\text{nm}^2$  but for the “standing” mode is (1.5x1.5)  $\text{nm}^2$ . Sauerbrey equation (2) calculates the monolayer coverage for the two possible orientations of collagen: **50Hz** for the “flat-on” mode and **11.180Hz** for the “standing” mode.

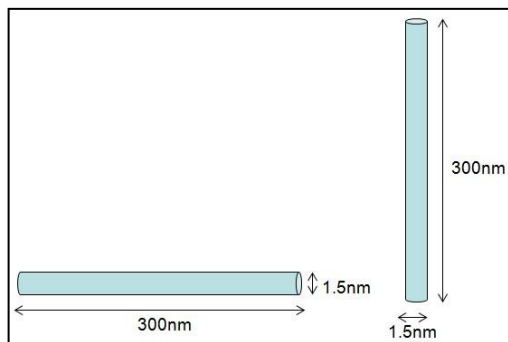


**Figure6.** The predicted orientations of a collagen molecule adsorbed on gold surface.

Collagen adsorption on Au surface seems to be concentration-dependent, as acoustic ratio varies within concentration changes. Collagen adsorption is a multi-step process as observed by the above experiments. At low concentrations collagen adopts a **flat** orientation, but at higher concentrations molecules take a more **vertical** or **tilted** orientation on Au (Fig.7).

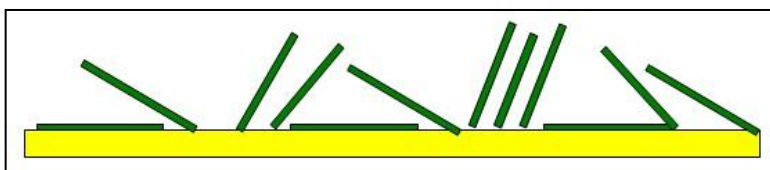


**Figure7.** Simulation of adsorbed collagen molecules on gold surface.

➤ **Fibronectin Adsorption**

Fibronectin adsorption studies were conducted on gold surfaces for various concentrations of fibronectin: 10, 40 and 50 ( $\mu\text{g}/\text{mL}$ ). Real-time graphs and D-f plots are given below (Fig.8) followed by a table of calculated average values (Table2).

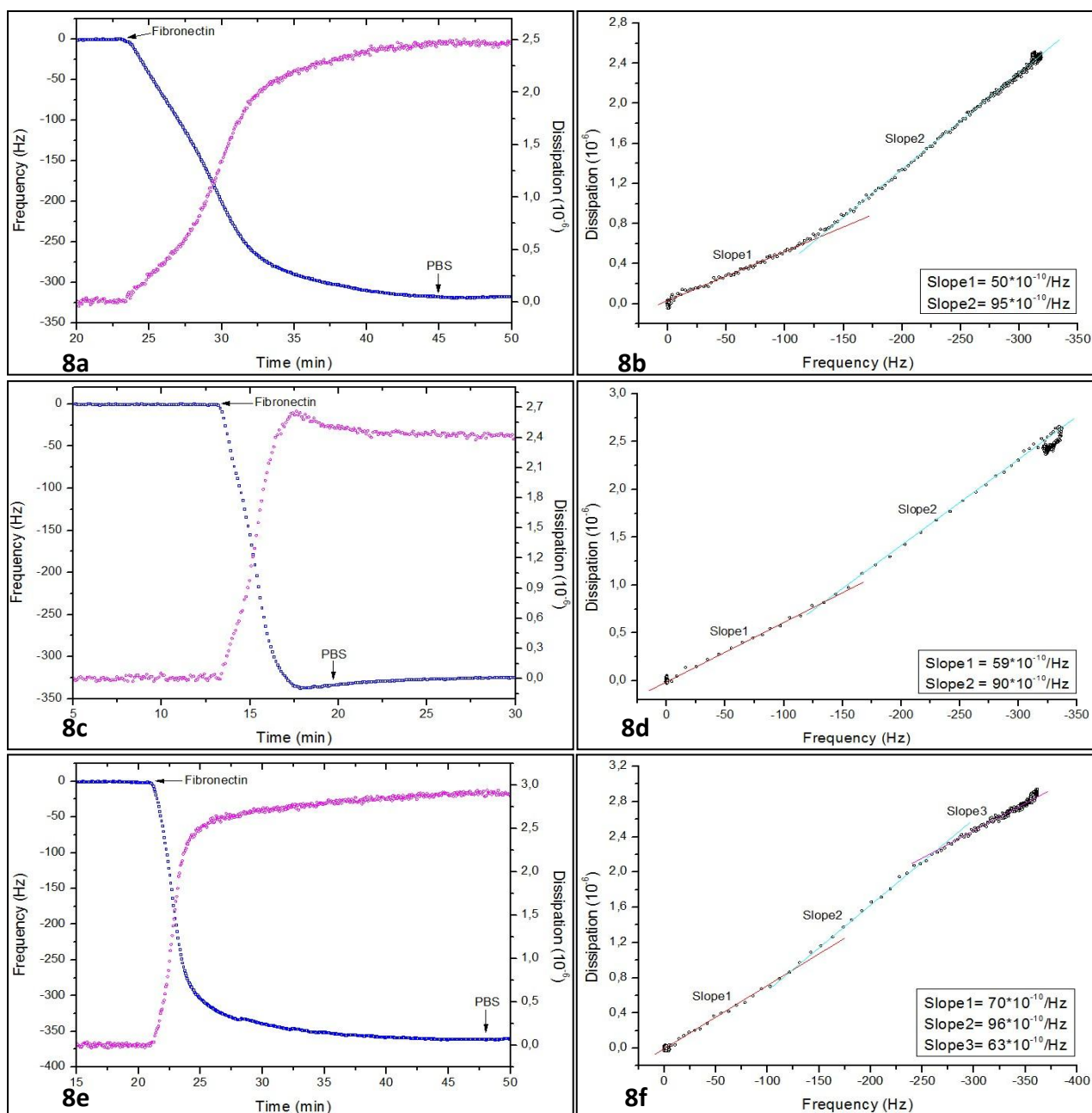


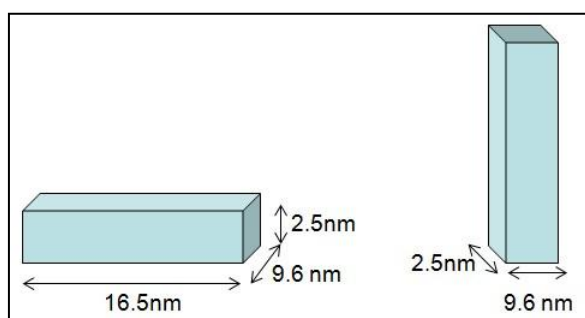
**Figure8.** Fibronectin adsorption real-time graphs (a, c, e) and D-f plots (b, d, f). Specifically, graphs depict adsorption of 10 $\mu\text{g}/\text{mL}$  (a and b), 40 $\mu\text{g}/\text{mL}$  (c and d) and 50 $\mu\text{g}/\text{mL}$  (e and f) of fibronectin on gold sensors.

Fibronectin concentration	$\Delta F$ (Hz)	$\Delta D$ ( $10^{-6}$ )	Slope1 ( $10^{-10}/\text{Hz}$ )	Slope2 ( $10^{-10}/\text{Hz}$ )	Slope3 ( $10^{-10}/\text{Hz}$ )	Number of experiments
10 $\mu\text{g}/\text{mL}$	315 $\pm$ 27	2.37 $\pm$ 0.15	50.75 $\pm$ 9.1	93.75 $\pm$ 1.89	-	4
40 $\mu\text{g}/\text{mL}$	392 $\pm$ 68	2.86 $\pm$ 0.55	52 $\pm$ 7	90 $\pm$ 5.5	-	3
50 $\mu\text{g}/\text{mL}$	409 $\pm$ 64	3.37 $\pm$ 0.65	62.5 $\pm$ 14.5	92 $\pm$ 2.6	94.75 $\pm$ 40	4

**Table2.** Average values of  $\Delta F$ ,  $\Delta D$  shifts and slopes of individual fibronectin adsorption experiments, compared for same experimental conditions.

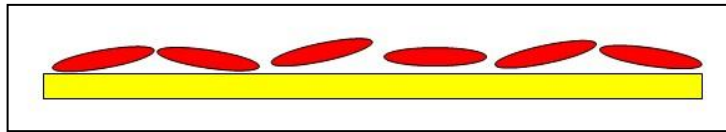
Real-time graphs (Fig.8a, c and e) of fibronectin adsorption depict frequency and dissipation shifts as a function of time;  $\Delta F$  and  $\Delta D$  shifts are represented with blue and magenta color respectively. Here, 10 $\mu\text{g}/\text{mL}$  (Fig.8b) and 40 $\mu\text{g}/\text{mL}$  (Fig.8d) concentrations of fibronectin used, resulted in a two-slope adsorption process. For 10 $\mu\text{g}/\text{mL}$  of fibronectin adsorption the acoustic ratios are  $\Delta D/\Delta F=50.75\pm 9.1$  ( $10^{-10}/\text{Hz}$ ) (slope1) and  $\Delta D/\Delta F=93.75\pm 1.89$  ( $10^{-10}/\text{Hz}$ ) (slope2). Also, 40 $\mu\text{g}/\text{mL}$  of fibronectin gave the acoustic ratio values:  $\Delta D/\Delta F=52\pm 7$  ( $10^{-10}/\text{Hz}$ ) (slope1) and  $\Delta D/\Delta F=90\pm 5.5$  ( $10^{-10}/\text{Hz}$ ) (slope2). In contrast, 50 $\mu\text{g}/\text{mL}$  (Fig.8f) of fibronectin adsorption resulted in three slopes, where acoustic ratio values are:  $\Delta D/\Delta F=62.5\pm 14.5$  ( $10^{-10}/\text{Hz}$ ) (slope1),  $\Delta D/\Delta F=92\pm 2.6$  ( $10^{-10}/\text{Hz}$ ) (slope2) and  $\Delta D/\Delta F=94.75\pm 40$  ( $10^{-10}/\text{Hz}$ ) (slope3). Notably, the three concentrations examined outcome two slopes with overlapping values, while the latter concentration presents a third slope with higher value.

Fibronectin molecular dimensions are (16.5x9.6x2.5) nm<sup>3</sup> and its molecular weight is 450kDa. The two putative orientations a fibronectin molecule can acquire when adsorbed on gold surface are: the “flat-on” and “standing” style. The footprint for the “standing” style is (9.6x2.5) nm<sup>2</sup>, while for the “flat-on” style there are two possible footprints; the (16.5x9.6) nm<sup>2</sup> and the (16.5x2.5) nm<sup>2</sup> (Fig.9). Sauerbrey equation (2) calculates the monolayer coverage for the two possible orientations of fibronectin: **190Hz** (footprint: (16.5x9.6) nm<sup>2</sup>), **720Hz** (footprint: (16.5x2.5) nm<sup>2</sup>) for the “flat-on” mode and **1200Hz** for the “standing” mode.



**Figure9.** The predicted orientations of a fibronectin molecule when adsorbed on gold surface.

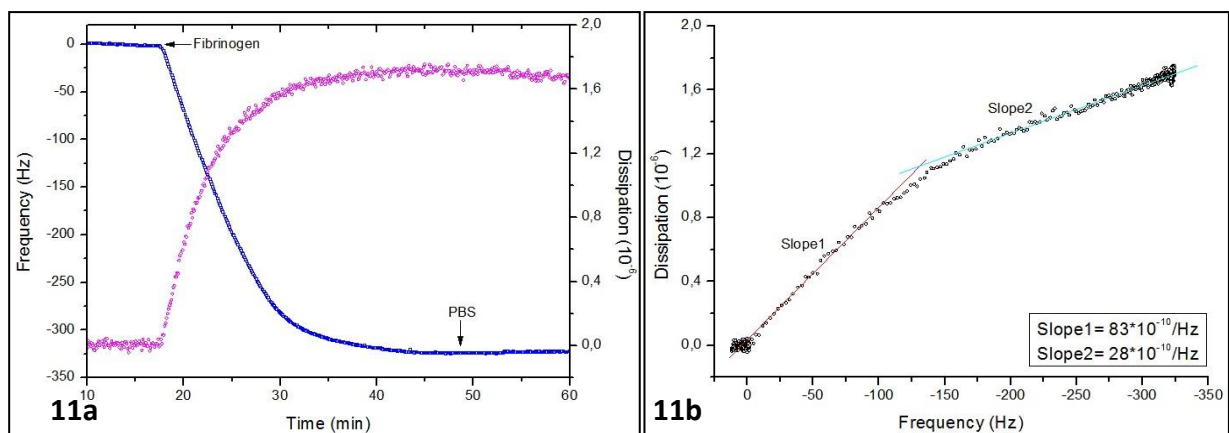
Fibronectin adsorption on Au surface seems to be concentration-dependent and is described by at least two slopes. Also, fibronectin seems to adopt a flat orientation on Au (Fig.10).



**Figure10.** Simulation of adsorbed fibronectin molecules on gold surface.

### ➤ Fibrinogen Adsorption

Fibrinogen adsorption studies were conducted for various concentrations of the molecule (10, 40 and 100 $\mu$ g/mL) on gold crystals. Real-time graphs and D-f plots of fibrinogen adsorption studies are given below and average values are summarized in Table3.



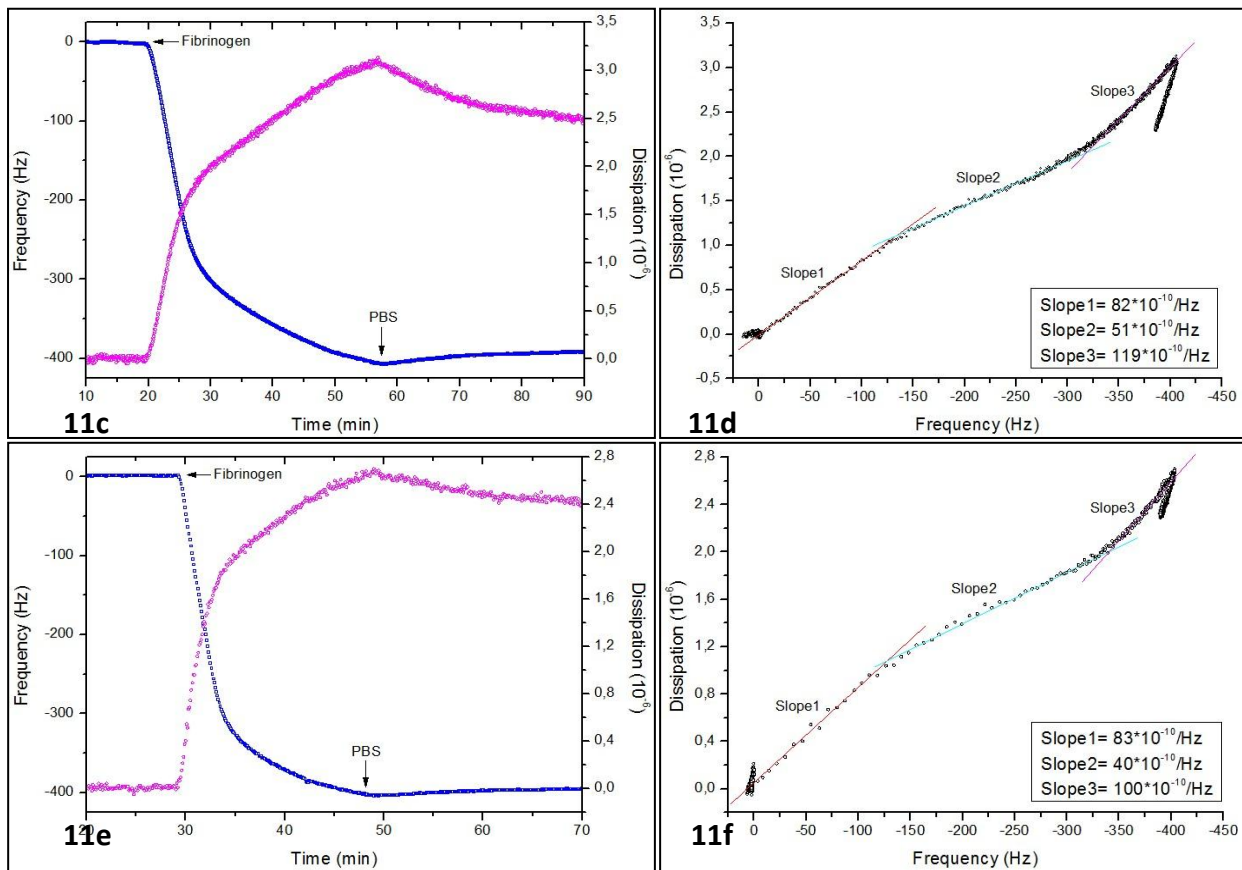


**Figure 11.** Fibrinogen adsorption real-time graphs (a, c, e) and D-f plots (b, d, f). Specifically, graphs depict adsorption of  $10\mu\text{g/mL}$  (a and b),  $40\mu\text{g/mL}$  (c and d) and  $100\mu\text{g/mL}$  (e and f) of fibrinogen on gold sensors.

Fibrinogen concentration	$\Delta F$ (Hz)	$\Delta D$ ( $10^{-6}$ )	Slope1 ( $10^{-10}/\text{Hz}$ )	Slope2 ( $10^{-10}/\text{Hz}$ )	Slope3 ( $10^{-10}/\text{Hz}$ )	Number of experiments
$10\mu\text{g/mL}$	$316\pm 15$	$1.67\pm 0.1$	$70.8\pm 9.3$	$32.1\pm 5.8$	-	17
$40\mu\text{g/mL}$	$370.5\pm 20.5$	$2.35\pm 0.21$	$91\pm 12.7$	$53.5\pm 3.5$	$120\pm 1.4$	2
$100\mu\text{g/mL}$	390	2.2	83	40	100	1

**Table 3.** Average values of  $\Delta F$ ,  $\Delta D$  shifts and slopes of individual fibrinogen adsorption experiments, compared for same experimental conditions.

Real-time graphs (Fig.11a, c and e) of fibrinogen adsorption depict frequency and dissipation shifts as a function of time;  $\Delta F$  and  $\Delta D$  shifts are represented with blue and magenta color respectively. For the three concentrations examined here, fibrinogen adsorption process can be described by at least two slopes. Specifically, for  $10\mu\text{g/mL}$  (Fig.11b) of fibrinogen adsorption two slopes are observed, with acoustic ratios  $\Delta D/\Delta F=70.8\pm 9.3$  ( $10^{-10}/\text{Hz}$ ) (slope1) and  $\Delta D/\Delta F=32.1\pm 5.8$  ( $10^{-10}/\text{Hz}$ ) (slope2). Fibrinogen adsorption for concentrations of  $40\mu\text{g/mL}$  (Fig.11d) can be described by three slopes with acoustic ratio values:  $\Delta D/\Delta F=91\pm 12.7$  ( $10^{-10}/\text{Hz}$ ) (slope1),  $\Delta D/\Delta F=53.5\pm 3.5$  ( $10^{-10}/\text{Hz}$ ) (slope2) and  $\Delta D/\Delta F=120\pm 1.4$  ( $10^{-10}/\text{Hz}$ ) (slope3).

Moreover, a single adsorption experiment of 100 $\mu\text{g}/\text{mL}$  (Fig.11f) fibrinogen claimed a three-slope process, where acoustic ratios are  $\Delta D/\Delta F=83$  ( $10^{-10}/\text{Hz}$ ) (slope1),  $\Delta D/\Delta F=40$  ( $10^{-10}/\text{Hz}$ ) (slope2) and  $\Delta D/\Delta F=100$  ( $10^{-10}/\text{Hz}$ ) (slope3). Interestingly, the two initial slopes values of 40 $\mu\text{g}/\text{mL}$  are slightly higher compared to those acquired from 10 $\mu\text{g}/\text{mL}$  fibrinogen adsorption. In contrast, 100 $\mu\text{g}/\text{mL}$  of fibrinogen adsorption resulted in two initial slopes with similar acoustic ratio values compared to those of the two-slope process of 10 $\mu\text{g}/\text{mL}$ .

Fibrinogen molecular dimensions are calculated as  $(45 \times 9 \times 6) \text{ nm}^3$  and its molecular weight 340kDa. When fibrinogen adsorbs on gold, it can take two possible orientations: the “flat-on” and the “standing” mode (Fig.12). The “standing” mode footprint dimensions are  $(9 \times 6) \text{ nm}^2$ . On the contrary, the “flat-on” mode gives two possible styles: the  $(45 \times 9) \text{ nm}^2$  and the  $(45 \times 6) \text{ nm}^2$  footprints. Using the Sauerbrey equation (2) the monolayer coverage for the “standing” mode was calculated **415Hz**, for the  $(45 \times 9) \text{ nm}^2$  footprint was **55Hz** and for the  $(45 \times 6) \text{ nm}^2$  footprint was **82Hz**.

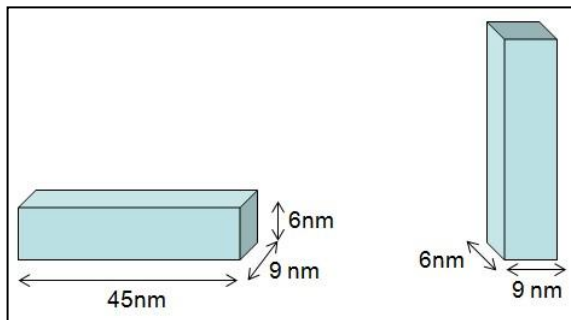


**Figure12.** Possible orientations of an adsorbed fibrinogen molecule on a gold surface.

Fibrinogen adsorption on gold surface seems to be a concentration-dependent phenomenon that can be described by at least two slopes. Based on the above, fibrinogen adopts a flat orientation when adsorbing on gold (Fig.13).

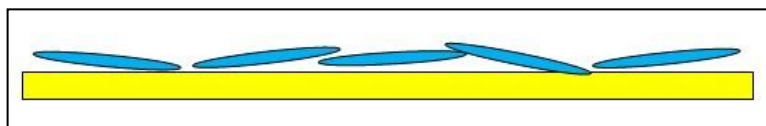


**Figure13.** Simulation of fibrinogen molecules adsorbed on gold surface.

## Cell adhesion studies

### ➤ Cell substrate selection

In order to perform cell adhesion studies on protein-coated gold sensors, the most appropriate protein substrate should be selected. In the beginning of protein adsorption on gold, proteins interact with the surface and this interaction depends on properties of the surface like hydrophobicity, hydrophilicity, morphology and roughness. There, proteins undergo conformational changes and as adsorption proceeds molecules rearrange to fit on the surface. Interactions of proteins adsorbed on gold with cells should be examined by a molecular point of view. Membrane receptors of cells interact with higher or lower affinity with their underlying substrates. Literature refers to many protein substrates for cell adhesion studies as mentioned in the introduction. Here, three extracellular proteins are examined regarding their ability to interact with two mammalian cell lines. The proteins used are collagen, fibronectin and fibrinogen, while the cell lines used are Nthy and ARO.

Collagen adsorbed on gold surface proved to be an unstable substrate for cell adhesion studies. In fact, Nthy and ARO cells adhered on collagen layer but could not stick on it, resulting in a positive frequency shift and a subsequent cell detachment from the coated surface (Fig.14).

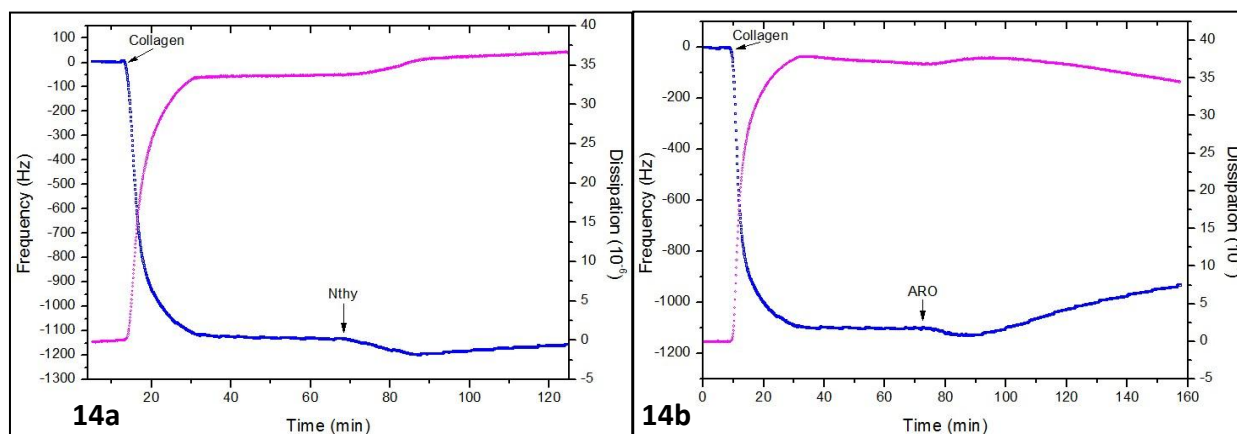


**Figure14.** Collagen ( $10\mu\text{g}/\text{mL}$ ) adsorbed on gold surface and then adhesion of a) Nthy cells ( $2 \cdot 10^5$  cells/mL) and b) ARO cells ( $2 \cdot 10^5$  cells/mL) at  $37^\circ\text{C}$ .

On the other hand, fibronectin was tested as a cell adhesion substrate. Cells could easily attach on fibronectin and yielded a significant  $\Delta f$  shift. The problem was that commercially available fibronectin molecule was really expensive and thus could not be utilized in a daily basis for cell adhesion studies. Thereby, a cost-effective and suitable substrate should be found. As fibrinogen is the major component of blood and many researchers use it for platelet adhesion studies, it constitutes an appropriate substrate to mimic natural microenvironments of cells. Based on the

above we investigated its interaction with thyroid cells. Fibrinogen has a really stable adsorption behavior; when interacting with cells gives clear and reliable results. So, in this study fibrinogen is the coating substrate that cells have to deal with.

➤ *Cell adhesion on fibrinogen-coated Au surface*

These cell adhesion studies were performed on fibrinogen-coated gold surface, at 25°C and with constant flow rate 30μL/min. In order to compare adhesion between Nthy and ARO cells, we measure ΔF and ΔD shifts for the first **50 minutes** of cell adhesion procedure.

In a typical biosensor experiment (Fig.15a) Nthy cells ( $2 \cdot 10^5$  cells/mL) adhere on fibrinogen-coated gold surface; ΔF, ΔD shifts are monitored in real-time and are depicted with blue and magenta color respectively. For these adhesion studies various concentrations of Nthy cells were examined ( $2 \cdot 10^4$ - $2 \cdot 10^5$  cells/mL). In Figure15 one can observe that as concentration of cells increase, the corresponding frequency (Fig.15b) and dissipation (Fig.15c) shift values are increased too. The ΔD/ΔF plot (Fig.15d) demonstrates a similar acoustic ratio value for every cell concentration.

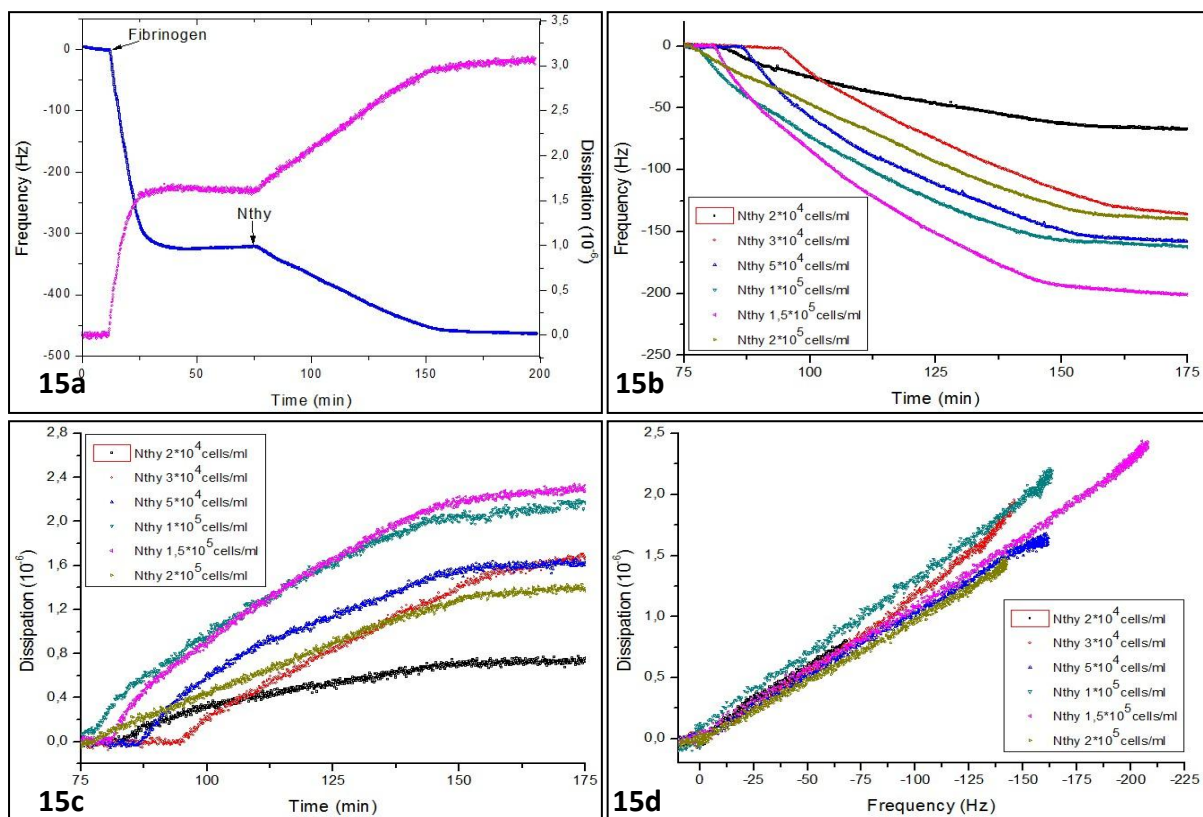


**Figure15.** Real-time plot (15a), ΔF plot (15b), ΔD plot (15c) and ΔD/ΔF plot (15d) for various concentrations of Nthy adhered on fibrinogen-coated gold surface at 25°C.

The same experiment was performed for various concentrations of ARO cells ( $2 \cdot 10^4$ - $2 \cdot 10^5$  cells/mL) in the same conditions. In a typical biosensor experiment, where ARO ( $2 \cdot 10^5$  cells/mL) adhere on fibrinogen-coated gold surface (Fig.16a),  $\Delta F$ ,  $\Delta D$  shifts are monitored in real-time and their signals are visualized with blue and magenta color respectively. Figure16 depicts the increase of  $\Delta F$  (Fig.16b) and  $\Delta D$  (Fig.16c) values as a function of the cell concentration increase. Also, similar acoustic ratio values were obtained for different cell concentrations (Fig.16d).

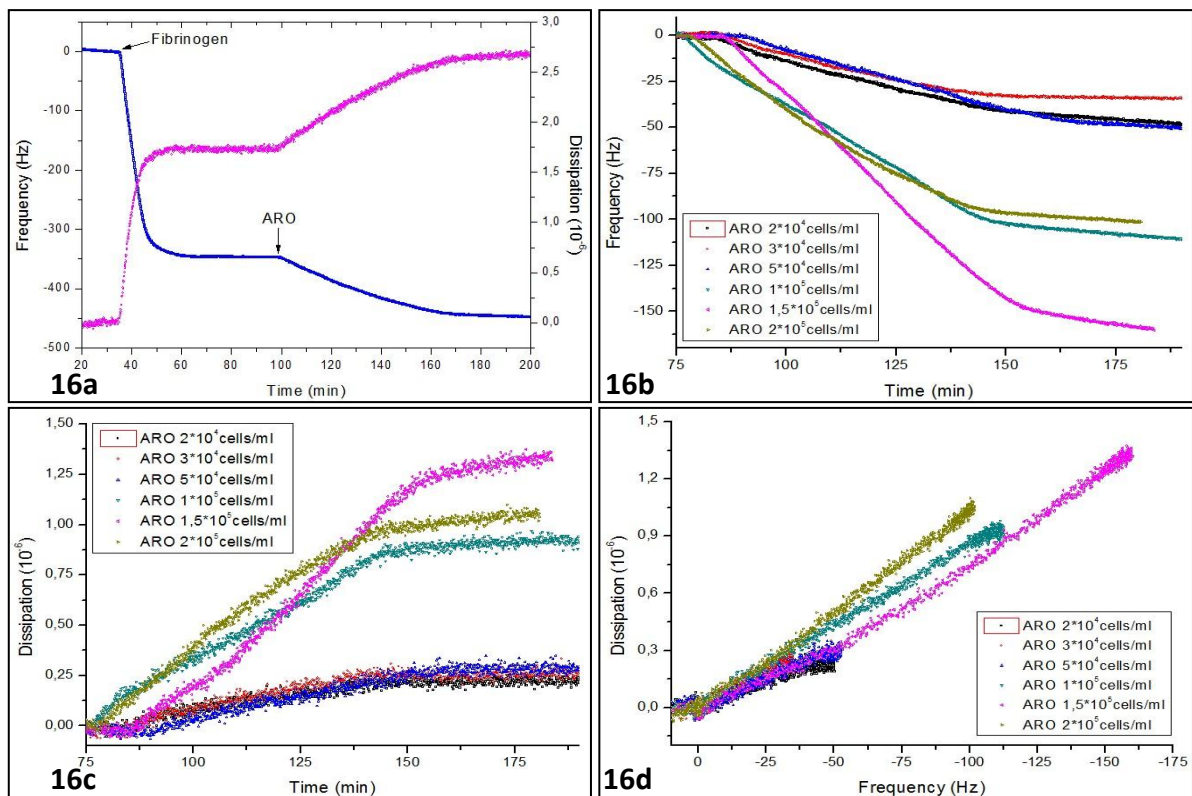


**Figure16.** Real-time plot (16a),  $\Delta F$  plot (16b),  $\Delta D$  plot (16c) and  $\Delta D/\Delta F$  plot (16d) for various concentrations of ARO adhered on fibrinogen-coated gold surface at 25°C.

Valuable information can be obtained by comparing the total  $\Delta F$  and  $\Delta D$  shifts values of the two cell lines for the initial 50 minutes of adhesion on fibrinogen-coated gold surface (Fig.17). The 50 minutes time period has been chosen for investigation of cell behavior prior to the buffer rinse.

For 50 minutes of cell adhesion procedure, ARO present smaller frequency (Fig.17a) and dissipation (Fig.17b) shifts than Nthy cells; the acoustic ratio (Fig.17c) remains constant about  $0.01 \cdot 10^{-6}/\text{Hz}$ . Especially for lower cell concentrations, ARO cells can be easily distinguished from Nthy ones from  $\Delta F$  and  $\Delta D$  shifts. Even though cell adhesion process did not reach equilibrium (plateau), cells responded quickly for this time point interval. Thus, 50 minutes of cell adhesion is an adequate time period

to trace binding and kinetics of cells and result in measurable differences between the two cell lines. A table summarizing the average values gained from this experiment can be found in appendix (**Table A**).

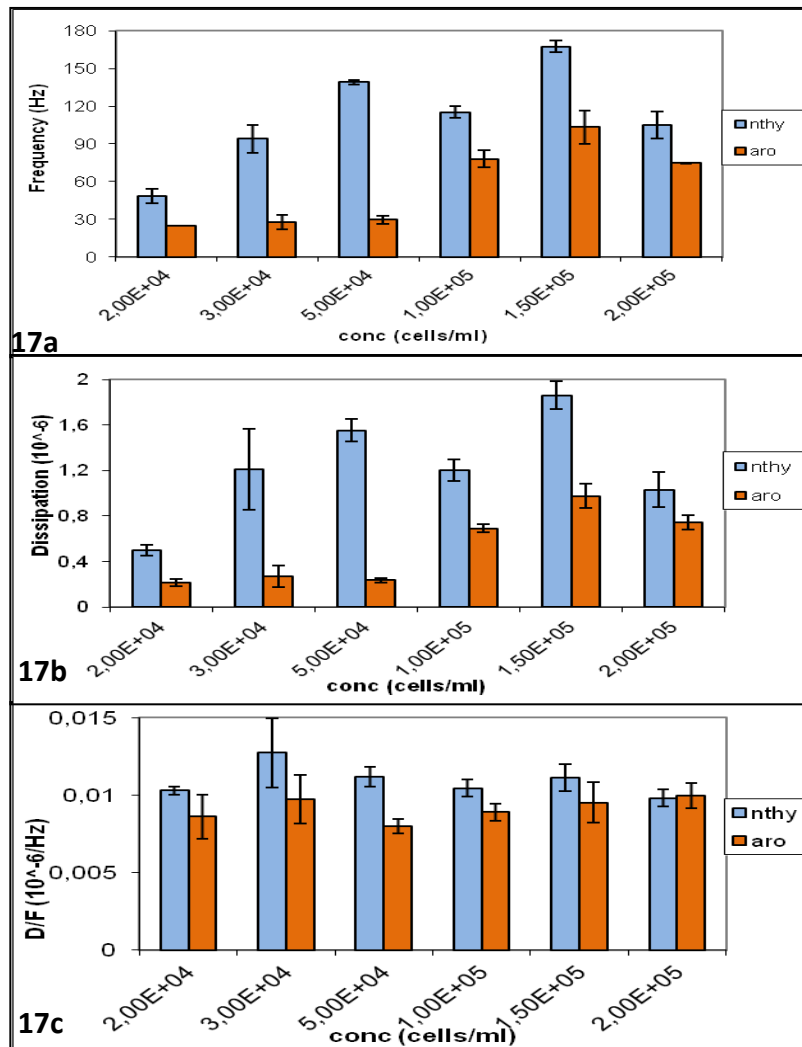


**Figure17.** Comparison of total  $\Delta F$  (17a),  $\Delta D$  (17b) and  $\Delta D/\Delta F$  (17c) values of Nthy and ARO cells obtained the initial 50 minutes of cell adhesion process, for the same cell suspensions and experimental conditions.

➤ *Cell adhesion on Au surface*

The adhesion studies of Nthy and ARO cells on uncoated (bare) gold surface were performed by MSc student Stratiotis Dimitrios to prove if there is an interaction of cells with the gold surface. Thereafter, using the same experimental conditions adhesion studies of the same cell lines on fibrinogen-coated gold surface were conducted (by MSc student Chronaki Dimitra) to investigate fingerprints of cells on general substrates. In this way, we would be aware of the interaction of cells with gold surface, which serves as a **control** for subsequent adhesion studies on protein substrates.

Binding isotherms of Nthy cells on gold surface for different cell concentrations ( $1 \cdot 10^3$ - $2 \cdot 10^5$  cells/ml) at equilibrium, were superimposed with the corresponding binding isotherms for the same cell line (concentrations:  $1 \cdot 10^4$ - $2 \cdot 10^5$  cells/ml) adhered on fibrinogen-coated gold surface at pseudo-equilibrium conditions. As concentration of cells adhering on gold surface increase, the frequency and dissipation values increase too, until they reach a plateau and remain constant.  $\Delta F$  (Fig.18a) and  $\Delta D$  (Fig.18b) average values as a function of each cell concentration are cited in the following figure.

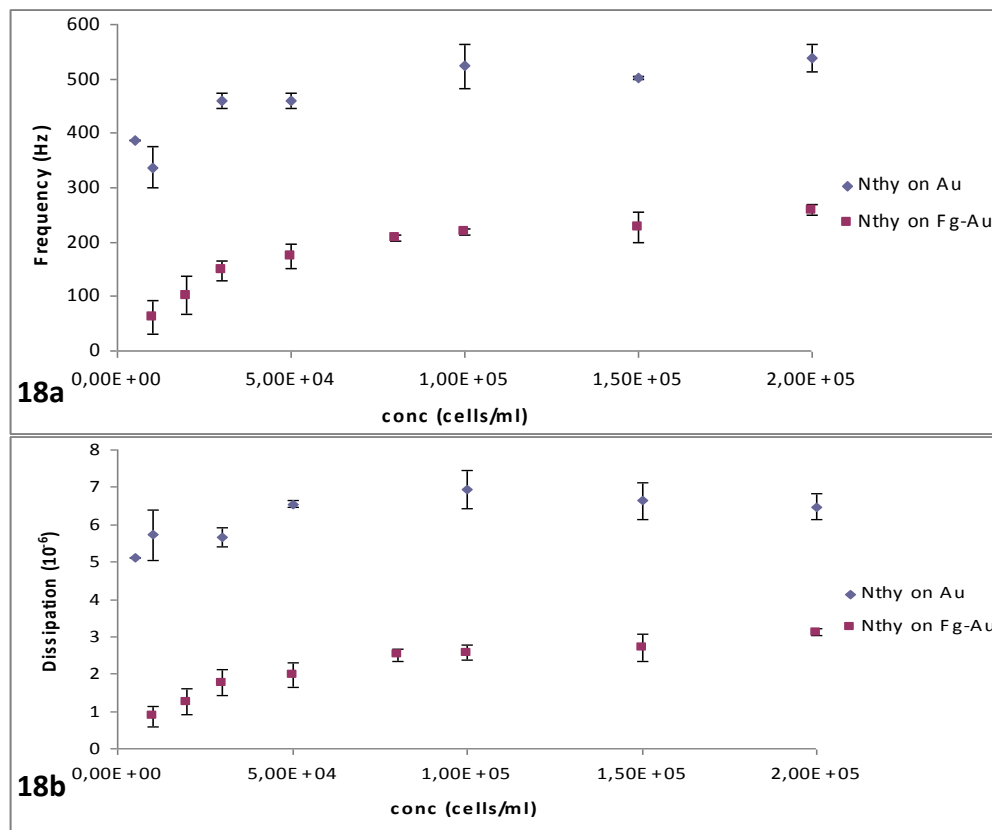


**Figure18.** Binding isotherms of Nthy cells on gold surface (blue color) and on fibrinogen-coated gold surface (red color) at 25°C.

Binding isotherms of the cell line ARO on gold surface for various cell suspensions ( $1 \cdot 10^3$ - $2 \cdot 10^5$  cells/ml) at equilibrium, were superimposed along with the binding isotherms of Nthy cells adhered on fibrinogen-coated gold surface at pseudo-equilibrium conditions (concentrations used:  $1 \cdot 10^4$ - $2 \cdot 10^5$  cells/ml). Here, as the concentration of cells adhering on gold surface increased, the corresponding frequency and dissipation values increased too, until the equilibrium. Average  $\Delta F$  (Fig.19a) and  $\Delta D$  (Fig.19b) shifts as a function of cell concentration are depicted in the figure below. Also, a table which summarizes the average  $\Delta F$  and  $\Delta D$  values can be found in the appendix (**Table B**).

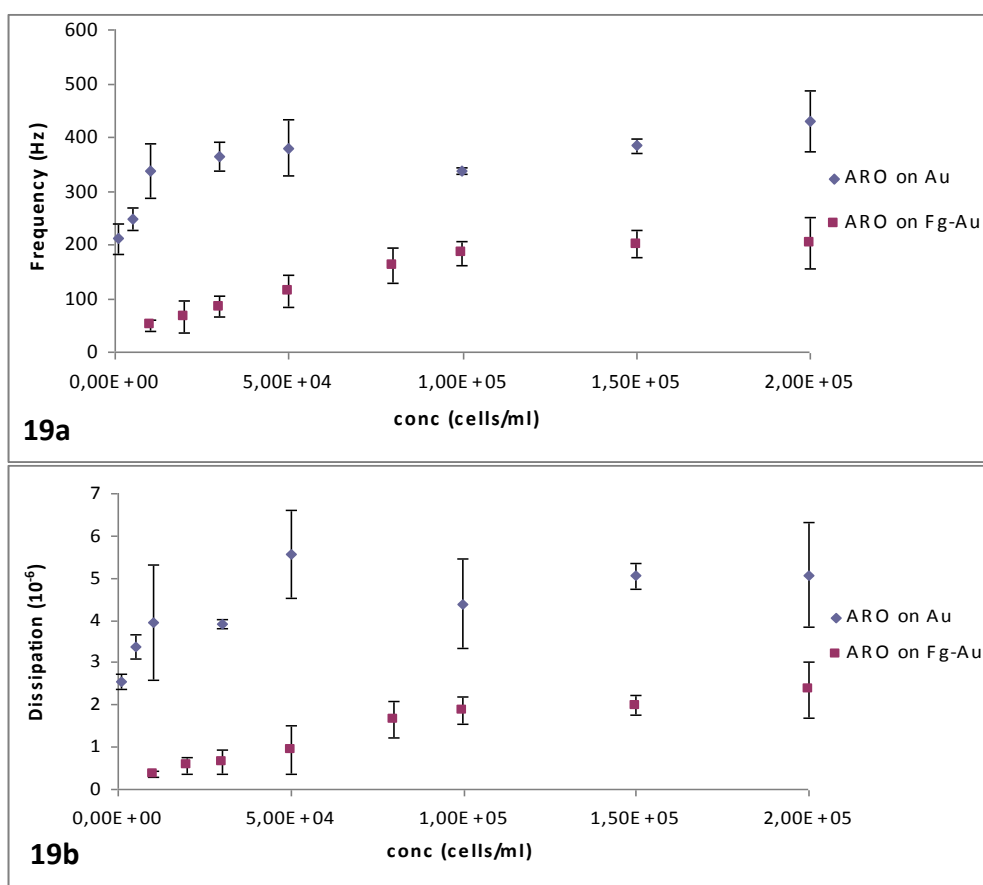


**Figure 19.** Binding isotherms of ARO cell line on gold surface (blue color) and on fibrinogen-coated gold surface (red color) at 25°C.

It is clear that both Nthy and ARO cells yield lower  $\Delta F$  and  $\Delta D$  signals when adhering on fibrinogen-coated gold than on bare gold (Fig.18, Fig.19). That could imply that the underlying substrate plays a major role for cell adhesion process.

➤ *Cell adhesion on fibrinogen-coated Au surface*

Cell adhesion studies of Nthy and ARO cells were conducted on fibrinogen-coated gold surface at 25°C with a constant flow rate 10μL/min. Here, a comparative analysis of the adhesion process of these two cell lines will be presented regarding the acquired ΔF and ΔD shift values.

A typical real-time biosensor experiment (Fig.20a) where Nthy cells ( $2 \cdot 10^5$  cells/mL) attach on fibrinogen-coated gold is described by ΔF and ΔD shifts; these shifts are depicted with blue and magenta color respectively. In this set of experiments, various suspensions ( $1 \cdot 10^4$  -  $2 \cdot 10^5$  cells/mL) of Nthy cells are used and the subsequent changes in frequency (Fig.20b) and dissipation (Fig.20c) signals are monitored. Notably, as cell concentration increase frequency and dissipation values increase too. Also, D/F plot (Fig.20d) depicts similar acoustic ratio values for the concentrations tested.

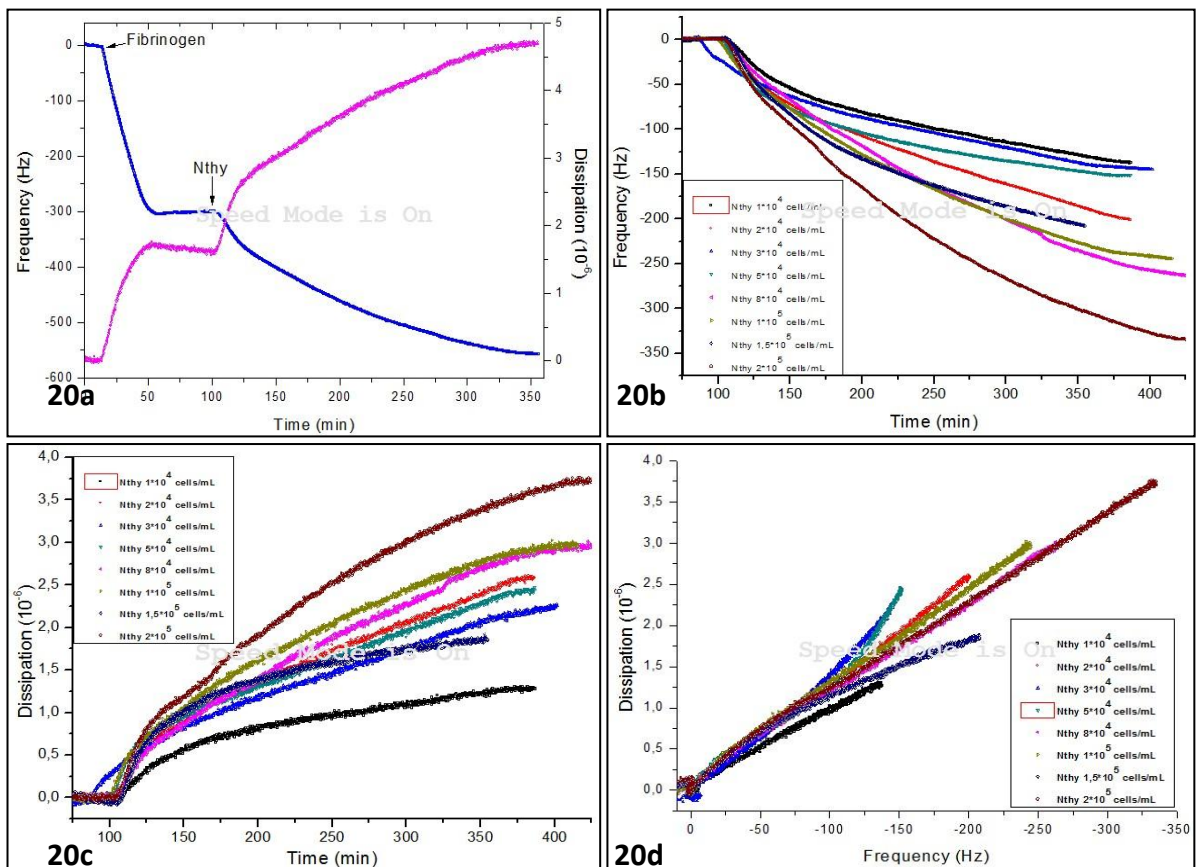


**Figure20.** Real-time plot (20a), ΔF plot (20b), ΔD plot (20c) and ΔD/ΔF plot (20d) for various concentrations of Nthy adhered on fibrinogen-coated gold surface at 25°C.

Cell adhesion experiments were conducted for the ARO cell line for various cell suspensions ( $1 \cdot 10^4$ - $2 \cdot 10^5$  cells/mL). Figure 21a represents a typical biosensing experiment with ARO cells ( $2 \cdot 10^5$  cells/mL) attaching on fibrinogen-coated gold and  $\Delta F$ ,  $\Delta D$  changes drawn with blue and magenta color respectively. Moreover, various concentrations of ARO cells cause different  $\Delta F$  (Fig. 21b) and  $\Delta D$  (Fig. 21c) shifts. Interestingly, different cell suspensions result in similar acoustic ratio values (Fig. 21d).

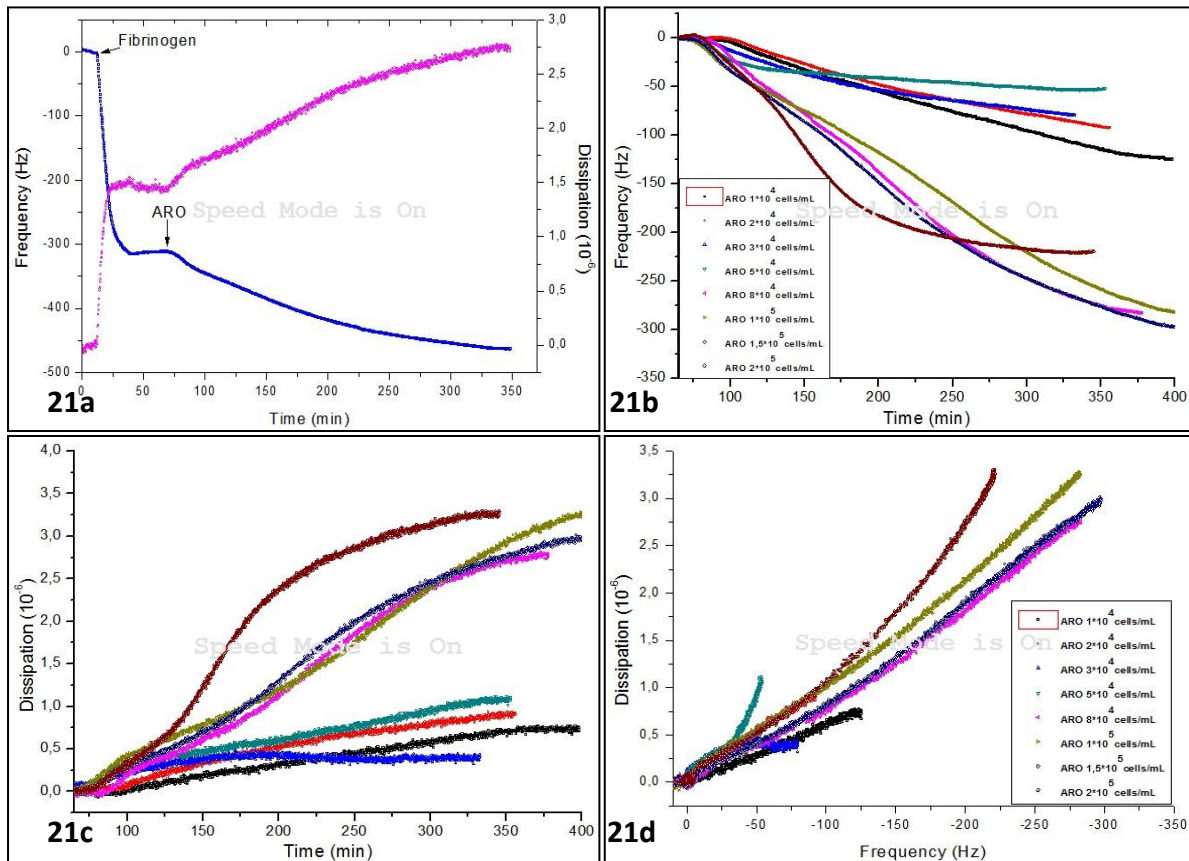


**Figure 21.** Real-time plot (21a),  $\Delta F$  plot (21b),  $\Delta D$  plot (21c) and  $\Delta D/\Delta F$  plot (21d) for various concentrations of ARO adhered on fibrinogen-coated gold surface at 25°C.

Cell adhesion experiments of Nthy and ARO cells performed on fibrinogen-coated gold using the same conditions result in measurable  $\Delta F$  and  $\Delta D$  shifts. In order to create binding isotherms of these two cell lines, we measure  $\Delta F$  and  $\Delta D$  shifts for the first **250 minutes** of cell adhesion process. Then, kinetic analysis of cell adhesion in parallel with optical microscopy imaging can supply us with additional information.

Binding isotherms for various concentrations ( $1 \cdot 10^4$ - $2 \cdot 10^5$  cells/mL) of Nthy and ARO cells adhering on fibrinogen-coated gold surface were created. Here, cell adhesion process did not reach a plateau for the time period studied. Thus, we

suppose that these cell adhesion studies are at pseudo-equilibrium conditions. As cell concentration increase, both frequency and dissipation values increase. Average  $\Delta F$  (Fig.22a) and  $\Delta D$  (Fig.22b) values for two cell lines are plotted versus cell concentration. In Figure22 one can observe that ARO average  $\Delta F$  and  $\Delta D$  values are lower than those of Nthy cells. Especially for lower concentrations of ARO average  $\Delta D$  values do not overlap with Nthy ones (Fig.22b). Additionally, the time interval of 250 minutes chosen for these experiments will be explained through kinetic analysis of the acquired data. A detailed table with average  $\Delta F$  and  $\Delta D$  values calculated by these experiments can be found in the appendix (**Table C**).

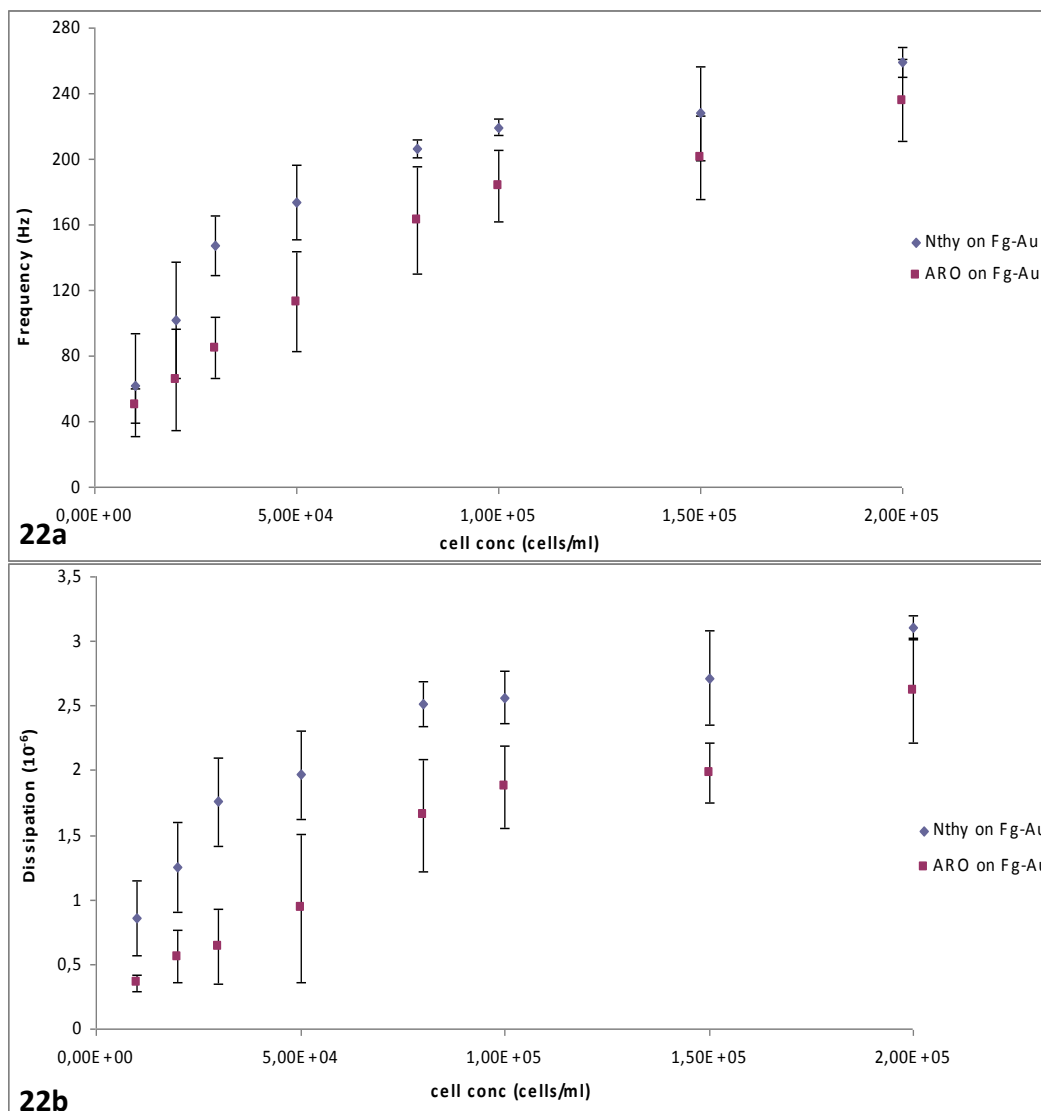


**Figure22.** Binding isotherms of Nthy (blue color) and ARO (red color) cell lines on fibrinogen coated surface at 25°C. Average  $\Delta F$  (22a) and  $\Delta D$  (22b) values of each cell line are plotted versus cell concentration.

➤ *Kinetic analysis of QCM-D data*

For a better understanding of QCM-D data, we fitted  $\Delta F$  data covering the whole period of cell adhesion process using the nonlinear regression analysis embedded in the OriginPro8 program. We observed that Nthy and ARO are characterized by single exponential decay (equation 3) which gives the best fits for  $\Delta F$  data:

$$Y = Y_0 + A1 * \exp(-t/\tau_1) \quad (3)$$

The above equation describes time ( $t$ ) dependent QCM responses ( $Y$ ). In this equation,  $Y_0$  is the maximum QCM response at  $t \rightarrow \infty$ , and  $A1$ ,  $\tau_1$ , the response lifetime, are the parameters to be fitted.

Cell adhesion curves of Nthy and ARO can be characterized by single exponential decay as seen in Fig.23. Exponential decay fitting is accompanied by a table summarizing the values of equation (3) which describes the exponential curve. Specifically, fitting of ARO and Nthy  $\Delta F$  data for same cell concentrations that result in similar theoretical equilibrium frequency values ( $Y = Y_0$ ) gives valuable information for cell adhesion kinetics. Figure23a presents the frequency shifts of Nthy (black curve) and ARO (red curve) (cell concentration is  $5 \cdot 10^4$  cells/mL) as a function of time, well-fitted by single exponential decay. Even if the adhesion of these two cell lines results in similar theoretical  $\Delta F$  values, the kinetics are different. Both cell lines exhibit an initial lag phase with  $\Delta F$  values that do not obey the equation (3). Also, adhesion of ARO seems to be a slower process than Nthy ones.

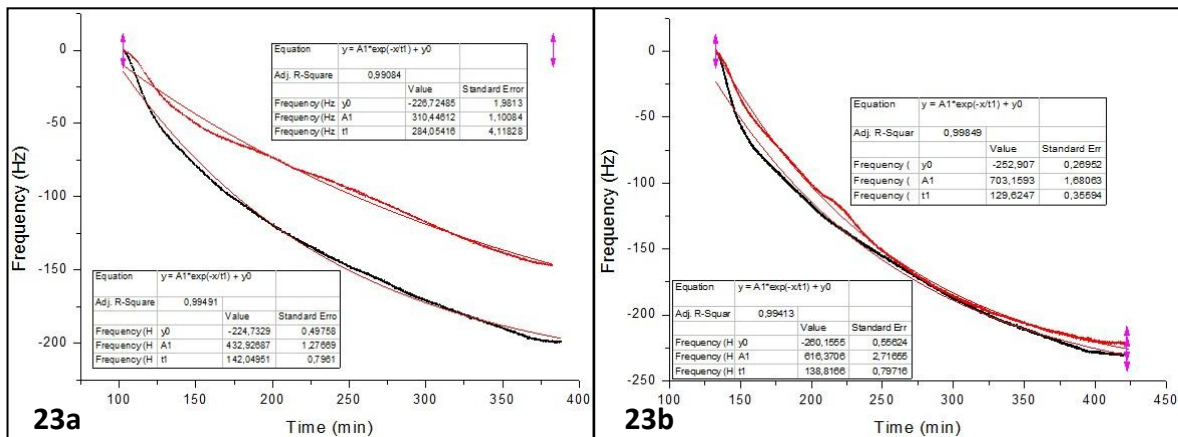


**Figure23.** Comparison of cell adhesion kinetics through exponential fitting: adhesion of Nthy (black curve) and summarizing table of exponential fit on the left and adhesion of ARO (red curve) and exponential fit summarizing table on the right. 23a) Adhesion of Nthy and ARO ( $5 \cdot 10^4$  cells/mL) while 23b) adhesion of Nthy and ARO ( $1.5 \cdot 10^5$  cells/mL).

Higher cell concentrations ( $1.5 \cdot 10^5$  cells/mL) of ARO (red curve) and Nthy (black curve) and the corresponding  $\Delta F$  shifts are presented in Fig.23b. These  $\Delta F$  data are also well-characterized by single exponential decay. For similar calculated theoretical

$\Delta F$  values these cell lines exhibit similar kinetic behavior. Also, the presence of an initial lag phase in adhesion process is obvious (Fig.23b). Interestingly, cell adhesion kinetics differs between low and high cell concentrations for the given experimental conditions. For low cell concentrations ARO seem to adhere slower than Nthy, whilst for higher concentrations the adhesion rate is the same.

As cell adhesion could not reach a plateau for the time period examined in this study, we further investigated how  $\Delta F$  signals would change as a function of time if the cell adhesion experiment continued for many more hours, using exponential decay fitting. The acquired  $\Delta F$  values for both cell lines can be fitted and calculated when  $t \rightarrow \infty$  ( $Y = Y_0$ ) (eq.3) to approximate the theoretical  $\Delta F$  values at equilibrium. In this way, we are able to correct the binding isotherms of Nthy and ARO cells (Fig.22a) created for the initial 250 minutes of cell adhesion process.  $\Delta F$  values depicted in Figure22a are considered as near the pseudo-plateau QCM responses. So, exponential decay fitting for both cell lines gives a better understanding of QCM signals at plateau conditions.

The acquired  $\Delta F$  values of Nthy and ARO cell adhesion experiments at pseudo-equilibrium conditions are calculated through equation (3) and corrected when  $Y = Y_0$ . Thus,  $\Delta F$  values in binding isotherms of Nthy and ARO cells are shifted. Specifically, in Nthy binding isotherm (Fig.24a) theoretical  $\Delta F$  values are higher than the experimentally calculated ones. For low cell concentrations ( $1 \cdot 10^4$ - $5 \cdot 10^4$  cells/mL), acquired and corrected data overlap, suggesting that these cell concentrations approximate plateau conditions for the 250 minutes experimental period. For higher cell concentrations ( $8 \cdot 10^4$ - $2 \cdot 10^5$  cells/mL) it is clear that experimental and corrected data do not agree, with higher corrected  $\Delta F$  values that do not even overlap with the experimental ones. This could suggest that higher cell concentrations are not able to easily reach a plateau for the 250 minutes time interval.

The aforementioned phenomenon occurs when correcting  $\Delta F$  values for ARO cell adhesion process. In Figure24b, acquired  $\Delta F$  values for low cell concentrations ( $1 \cdot 10^4$ - $3 \cdot 10^4$  cells/mL) are in good agreement with the corrected ones while the acquired  $\Delta F$  values for higher cell concentrations ( $5 \cdot 10^4$ - $2 \cdot 10^5$  cells/mL) are really lower than the corrected ones. As mentioned for the Nthy cell line, ARO cell adhesion can easily reach a plateau for low cell concentrations, but for higher concentrations this does not happen.

The binding isotherm of Nthy and ARO cells presented in Figure22a is now corrected through exponential decay fitting and average  $\Delta F$  values for various cell concentrations are depicted in Figure24c. In this figure, ARO cell line presents lower average  $\Delta F$  values when compared with Nthy ones, for different cell concentrations.

Average  $\Delta F$  values (corrected) used for the below binding isotherms are summarized in the appendix (Table D).

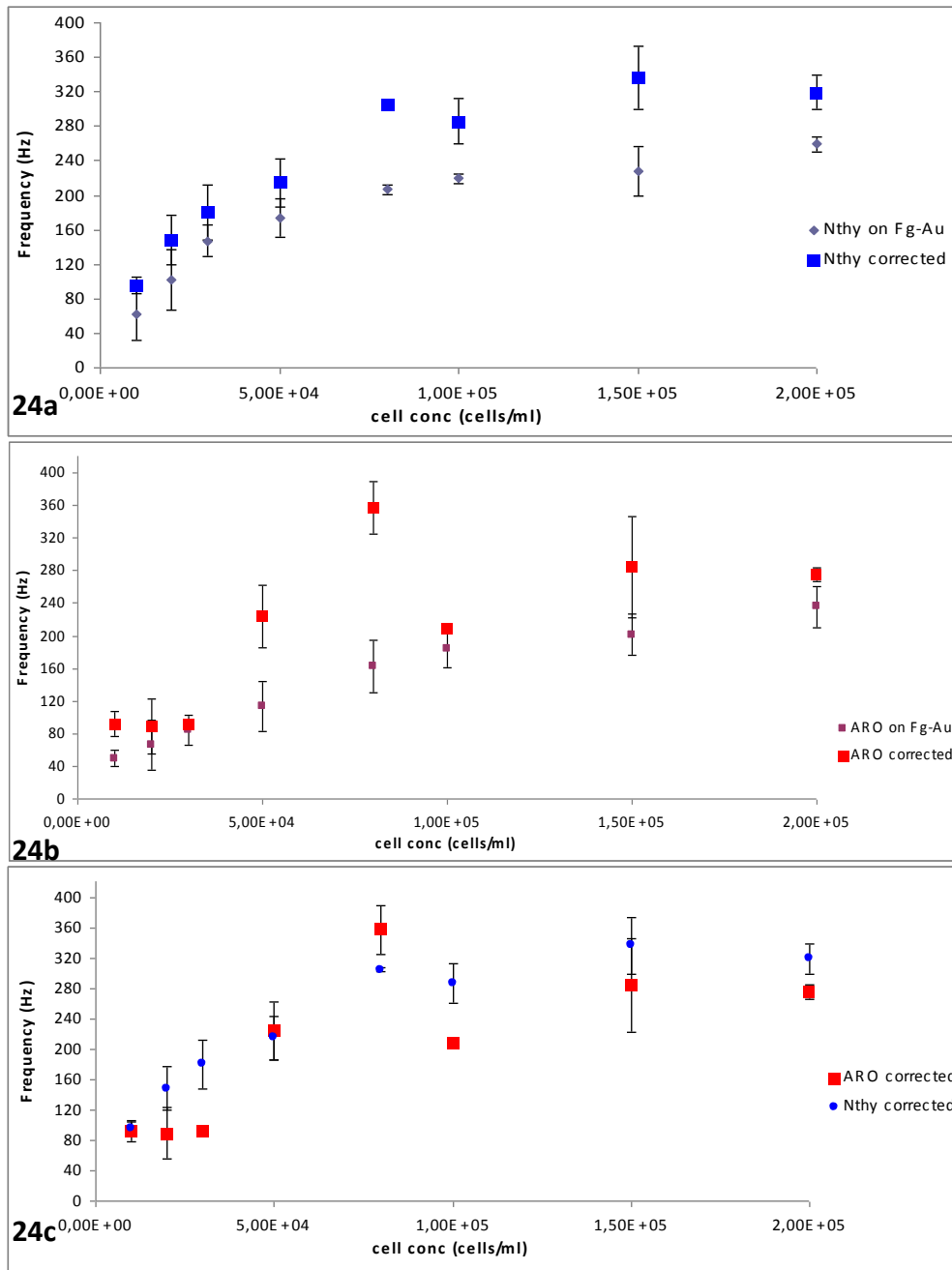


**Figure24.** Binding isotherms with corrected average  $\Delta F$  values; Nthy binding isotherm (24a), ARO binding isotherm (24b) and superimpose of the above binding isotherms (24c).

➤ *Optical microscopy images*

At the end of cell adhesion experiments gold sensors were observed by light microscopy technique. Light microscopy managed to capture the image of gold sensors after the cell adhesion process. Usually, 10x magnification was used to gain the overall image of sensor areas, while the 20x magnification to record shape and morphology of attached cells. Moreover, distribution of cells on sensor areas was varying within the same experiment; some areas were fully covered with cells and others were unoccupied.

Cell adhesion images of Nthy, ARO cells ( $1 \cdot 10^5$  cells/mL) on fibrinogen-coated sensors at 25°C and with flow rate 30  $\mu$ L/min are cited in Figure25. Nthy cells appear to have two different morphologies on fibrinogen-coated sensors: round ( $\approx 20$ -35  $\mu$ m diameter) and flattened round ( $\approx 50$   $\mu$ m diameter) (Fig.25: middle panel, red boxes). In contrast, ARO cells appear only as rounded cells with an approximate diameter of 15-25  $\mu$ m (Fig.25: middle panel, blue box).

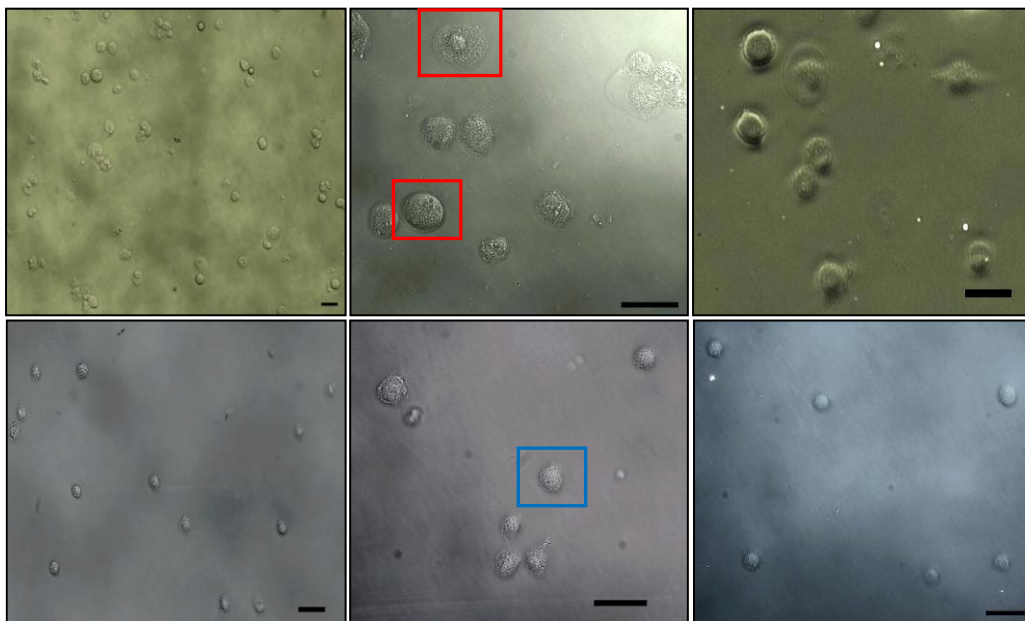


**Figure25.** Light microscope images of cell adhesion experiments on gold sensors. **Above panel:** Nthy ( $1 \cdot 10^5$  cells/mL), 10x magnification of adhesion area (left panel), 20x magnification of adhesion area (middle and right panel). **Below panel:** ARO ( $1 \cdot 10^5$  cells/mL), 10x magnification of adhesion area (left panel), 20x magnification of adhesion area (middle and right panel). Scale bars: 50  $\mu$ m.

On the top of that, cell adhesion images of Nthy, ARO cells ( $2 \cdot 10^5$  cells/mL) on fibrinogen-coated sensors at 25°C and with flow rate 10  $\mu$ L/min are cited in Figure26. Here, Nthy seem to adopt a rounded morphology which is approximately 20-40  $\mu$ m in diameter (Fig.26: right panel, red box). As stated before ARO have a rounded morphology ( $\approx 15$ -30  $\mu$ m diameter) (Fig.26: right panel, blue box).

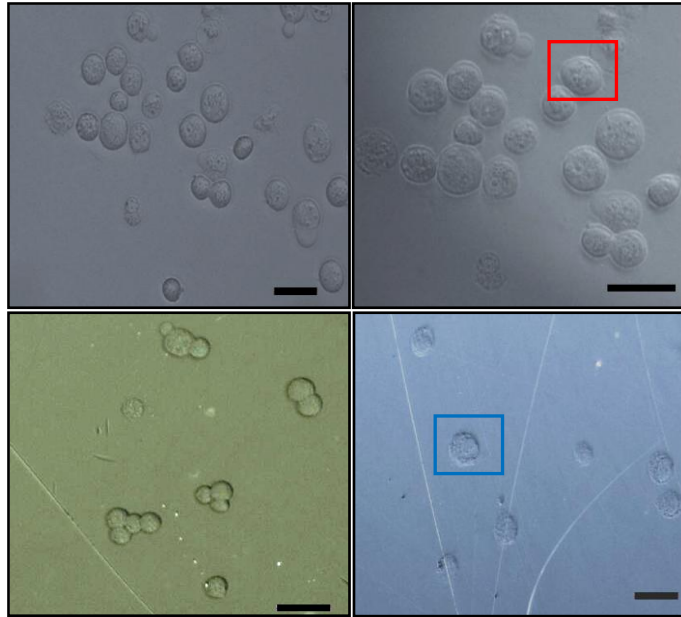


**Figure26.** Light microscope images of cell adhesion experiments on gold sensors. **Above panel:** Nthy ( $2 \cdot 10^5$  cells/mL), 10x magnification of adhesion area (left panel) and 20x magnification of adhesion area (right panel). **Below panel:** ARO ( $2 \cdot 10^5$  cells/mL), 10x magnification of adhesion area (left and right panel). Scale bars:  $50 \mu\text{m}$ .

Additional information can be gained from cell adhesion images of Nthy, ARO cells ( $1.5 \cdot 10^5$  cells/mL) on fibrinogen-coated **artificial** sensor surfaces at  $25^\circ\text{C}$  and with flow rate  $10 \mu\text{L}/\text{min}$  (Fig.27). Here, Nthy adopt a rounded morphology ( $\approx 20\text{-}35 \mu\text{m}$  in diameter) (Fig.27: left panel, red box). Also, ARO seem to have the same rounded morphology ( $\approx 15\text{-}25 \mu\text{m}$  in diameter) as in previous experiments (Fig.27: right panel, blue box). These artificial surfaces can easily simulate the gold sensors' surfaces and surface properties regarding the morphology of the adhered cells.

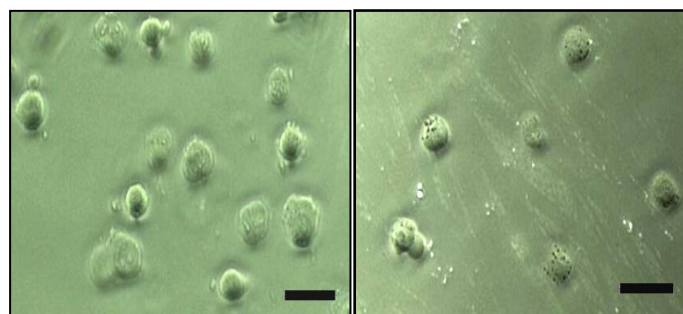


**Figure27.** Light microscope images of cell adhesion on artificial gold sensors. **Left panel:** Nthy ( $1.5 \cdot 10^5$  cells/mL), 10x magnification of adhesion area. **Right panel:** ARO ( $1.5 \cdot 10^5$  cells/mL), 10x magnification of adhesion area. Scale bars:  $50 \mu\text{m}$ .

## ➤ RGD peptides

In order to investigate whether RGD peptides interact with adhered cells or with their underlying substrate, we performed three control experiments:

### 1. Interaction of RGDs with fibrinogen-coated gold surface

Excess of RGD peptide solution was inserted in a fibrinogen layer on gold surface and yielded no significant response. In fact, RGDs do not interact with fibrinogen molecules and thus we do not observe changes in dissipation and frequency signals (Fig.28).

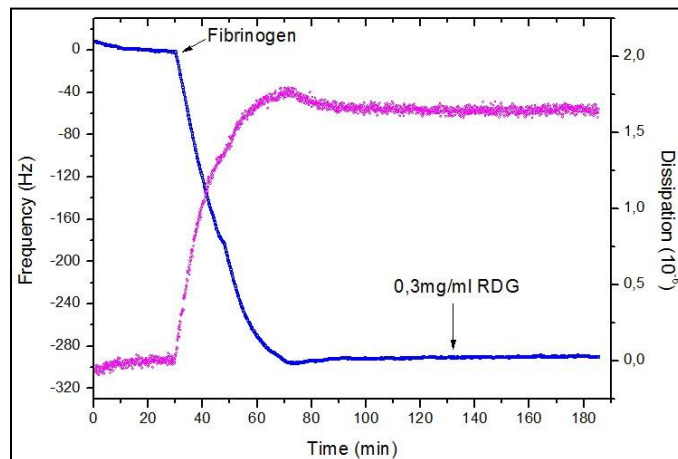


**Figure28.** Addition of 0.3mg/mL RGD peptide solution on fibrinogen-coated gold surface at 25°C.

### 2. Interaction of RGD pre-incubated cells with fibrinogen-coated gold surface

In this experiment, Nthy cells adhere on fibrinogen-coated gold surface (control). Nthy cells (20.000cells/mL) pre-incubated with 100 $\mu$ g/mL RGD peptide adhere on fibrinogen-coated gold surface too. Nthy cells pre-incubated with RGD peptide display the same behavior as the ones not pre-incubated with the peptide (Fig.29). This can imply that RGDs are not able to interact with Nthy cells and block or reduce their binding on fibrinogen.

One could assume that any positive or negative frequency change could imply blocking or binding of cells respectively. These changes could not occur due to RGD peptide binding on fibrinogen as RGDs do not interact with it (Fig.28). So, RGDs are not capable of altering Nthy cell binding on fibrinogen for the given experimental conditions.

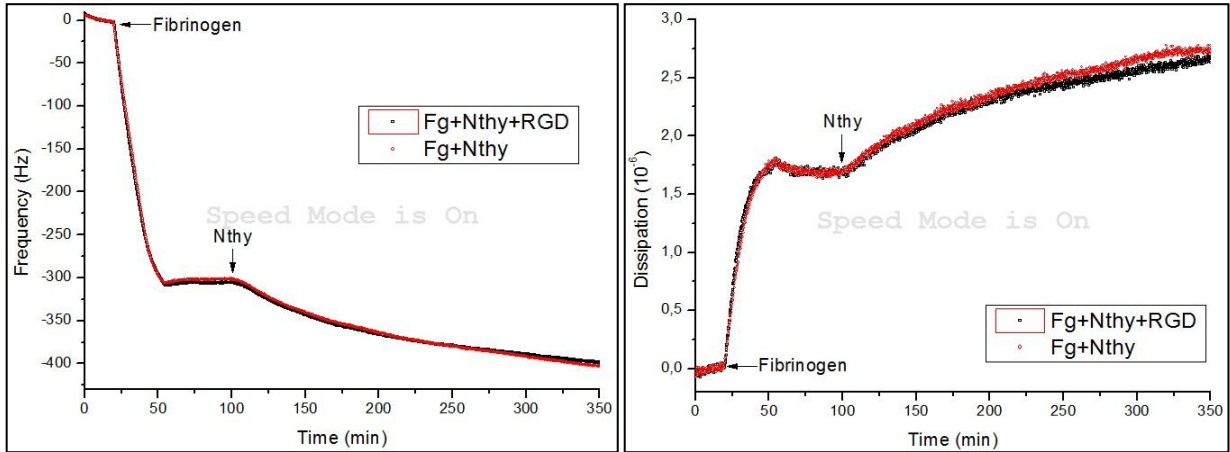


**Figure29.** Frequency and dissipation shifts of the adhesion of Nthy (20.000cells/mL) a) pre- incubated with 100 $\mu$ g/mL RGD peptide (black line) and b) without addition of peptide (red line) on fibrinogen-coated gold at 25°C.

### 3. Interaction of RGD peptides with adhered cells on fibrinogen-coated gold surface

RGD peptide solution with a concentration of 100 $\mu$ g/mL was inserted in the flow chamber at the end of a cell adhesion experiment, were ARO (20.000cells/mL) adhered on fibrinogen-coated gold. RGD peptides did not manage to detach cells from the protein layer or bind on them. Though, RGDs caused slight changes in the viscoelastic behavior of the system for several minutes until equilibrium restored (Fig.30).

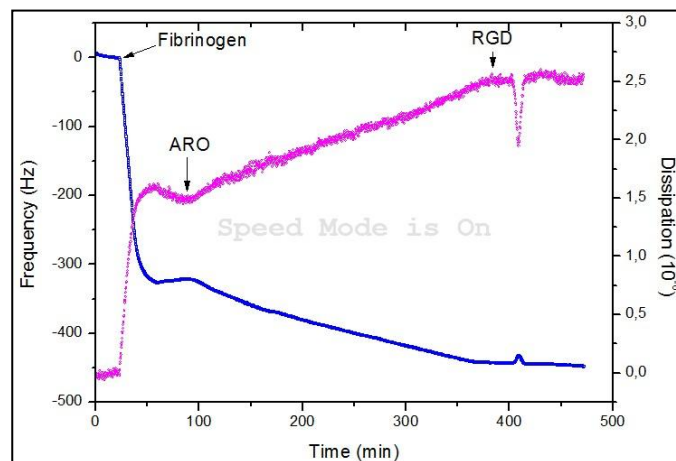


**Figure30.** Addition of 100 $\mu$ g/mL RGD peptide solution on adhered ARO cells (20.000cells/mL) and the corresponding frequency and dissipation shifts.

## CHAPTER 4

### DISCUSSION

---

Protein adsorption studies were performed using three extracellular proteins of medical interest: collagen, fibronectin and fibrinogen. Adsorption of proteins on gold surface is traced by QCM-D technique and the results are interpreted quantitatively and qualitatively. The qualitative explanation of results lies on the “discrete molecule” theory, where molecules adsorbing on a surface behave as discrete molecules and not as a homogenous viscoelastic film [66-68]. This molecular approach can provide us with information about size, shape and conformation of adsorbed molecules.

Collagen adsorption studies revealed that collagen gives high frequency and dissipation shifts when adsorbing on gold surface. Three concentrations of collagen were examined and proved that collagen adsorption process is concentration-dependent. The adsorption of low collagen concentrations (5, 10  $\mu\text{g}/\text{mL}$ ) can be described by two slopes with similar values. For the initial  $\Delta F = 100\text{Hz}$  of collagen adsorption the acoustic ratio remains constant (Slope1), while the following 600Hz described by Slope2 (Fig.5b, Fig.5d). Higher concentrations (40 $\mu\text{g}/\text{mL}$ ) result in a multi-slope adsorption process. Notably, the two initial slopes have similar values as lower collagen concentrations. When  $\Delta F$  exceeds 700Hz, acoustic ratio remains constant (Slope3) (Fig.5f). A fourth slope is observed in Fig.5f maybe due to the formation of a bilayer of collagen molecules.

Moreover, collagen layers seem to be soft and viscoelastic as collagen adsorption is described by high dissipation shifts [2, 6]. If we neglect the dissipative nature of collagen, Sauerbrey equation (2) could calculate the monolayer coverage for the two possible orientations of collagen on gold surface. The “flat-on” mode of collagen would give a full monolayer coverage for  $\Delta F = 50\text{Hz}$ , while the “standing” mode would give a coverage for  $\Delta F = 11.180\text{Hz}$  (Fig.6). The acquired  $\Delta F$  values combined with the acoustic ratio measurements suggest that collagen initially adopts a **flat** orientation on gold ( $\Delta D/\Delta F \approx 100 \cdot 10^{-10}/\text{Hz}$ ) and higher density of molecules probably lead to rearrangements so that molecules adopt a **vertical/tilted** orientation on gold (higher  $\Delta D/\Delta F$  ratios) (Fig.7). Nezu et al [3] suggest that collagen molecules slightly change their structure in the course of adsorption, while seeking the thermodynamically most stable conformation. During collagen adsorption molecules first create a thin mat on the surface and then a thicker overlayer ( $\approx 200\text{nm}$ ) with protruding molecules in a very low concentration [5]. Furthermore, collagen did not behave as an appropriate substrate for cell adhesion as cells detached from the surface when interacting with collagen molecules (Fig.14). This may occur because

collagen creates a really viscoelastic layer, with high water content (70±20% water [2, 5, 6]) that cannot serve as a platform for cell binding (for the cell lines tested here).

Fibronectin adsorption studies conducted on gold surface yielded significant frequency and dissipation shifts but still lower than those of collagen. Three concentrations of fibronectin were tested, proving that the adsorption process is a concentration-dependent phenomenon described by at least two slopes. Indeed, 10 and 40µg/mL of fibronectin resulted in two slopes with acoustic ratio values:  $\Delta D/\Delta F \approx 50 \cdot 10^{-10}/\text{Hz}$  and  $\Delta D/\Delta F \approx 90 \cdot 10^{-10}/\text{Hz}$ , for the initial 100Hz and later 150Hz respectively (Fig.8b, Fig.8d). Higher fibronectin concentration 50µg/mL resulted in two similar slopes for the above estimated frequency shifts and a third slope with an acoustic ratio value  $\Delta D/\Delta F \approx 94.75 \pm 40 \cdot 10^{-10}/\text{Hz}$  (Fig.8f). Additionally, as fibronectin layers are thin and nondissipative they obey Sauerbrey equation (2) which calculates the monolayer coverage for the “standing” mode to be 1200Hz and for the “flat-on” mode 190Hz or 720Hz (Fig.9). Acoustic ratio measurements and deposited mass which is both above and below the estimated monolayer coverage, suggest that fibronectin molecules adopt a **tight flat** orientation on gold surface (Fig.10).

Fibronectin is considered to adsorb on hydrophilic surfaces as a soft, less rigid protein layer in contrast to the more rigid, densely packed layer on hydrophobic surfaces [18]. Giambianco et al [16] claim that adsorbed fibronectin molecules on PHMS adopt a **flat-on** conformation with most domains in close contact with the surface and that pure fibronectin layer has an acoustic ratio value  $\Delta D/\Delta F = 6.2 \cdot 10^{-8}$ . Also, low  $\Delta D/\Delta F$  values suggest that fibronectin film is compact [20]. These publications reinforce our estimation that fibronectin adopts a compact flat orientation on gold surface.

Fibrinogen adsorption produced frequency and dissipation shifts approximating those of fibronectin, but really lower than collagen ones. Indeed fibrinogen layers include 50±10% water and are less viscoelastic than collagen layers [2]. In general, fibrinogen adsorption process can be described by two slopes with acoustic ratio values  $\Delta D/\Delta F \approx 80 \cdot 10^{-10}/\text{Hz}$  (Slope1) and  $\Delta D/\Delta F \approx 40 \cdot 10^{-10}/\text{Hz}$  for the initial 100Hz and the following 200Hz respectively (Fig.11b). Higher fibrinogen concentrations produce a third slope with higher acoustic ratio value of  $\Delta D/\Delta F \approx 100 \cdot 10^{-10}/\text{Hz}$  (Fig.11d, Fig.11f). Thus, fibrinogen adsorption process is concentration-dependent. Fibrinogen layers are considered as thin and nondissipative (small dissipation shifts monitored) and can obey Sauerbrey equation (2). The calculated monolayer coverage for the “standing” style of fibrinogen molecules was 415Hz while for the “flat-on” style was 55Hz or 82Hz (Fig.12). Combining acoustic ratio values with the calculated monolayer coverage we assume than fibrinogen molecules adopt a **flat** orientation on gold

(Fig.13). Hemmersam et al [19] propose that for low fibrinogen concentrations (0.033mg/mL) molecules have time to interact with the surface resulting in a tight-bound layer, while for higher concentrations (1mg/mL) fibrinogen molecules are loosely bound to the surface. In addition, fibrinogen adsorption (10 $\mu$ g/mL) resulted in very stable  $\Delta D/\Delta F$  values (Slope2) within the individual experiments, implying a firm orientation of the underlying layer which served as a platform for cell adhesion studies.

Cell adhesion studies recruited QCM-D technology to distinguish the dynamic cell adhesion signatures of human normal (Nthy.ori 3-1) versus malignant (ARO) thyroid cells. QCM-D responses are correlated with cell adhesion kinetics and cell morphology as observed by optical microscopy.

Primary cell adhesion experiments were designed to investigate the interaction of Nthy and ARO cells with fibrinogen-coated gold surface. In these experiments, cell-substrate interaction was performed under 30 $\mu$ L/min flow rate, frequency and dissipation shifts were monitored for the first 50 minutes of cell adhesion procedure (Fig.15, Fig.16). The outcome of this experiment is that ARO produce lower average frequency and dissipation shifts than Nthy cells for 50 minutes of cell adhesion, while the acoustic ratio remains constant  $\Delta D/\Delta F \approx 0.01 \cdot 10^{-6}/\text{Hz}$  (Fig.17). For lower cell concentrations it is easier to discriminate these two cell lines. These primary results suggest that ARO cells exhibit a reduced binding capacity and have different viscoelastic properties compared to Nthy. Moreover, 50 minutes proved a sufficient time interval in order to gain measurable signals and distinguish the two cell lines. This type of cell adhesion experiment could be used as a tool to trace binding of different thyroid cell lines. The advantage of such approach is that the use of a quick flow rate, instead of 10 $\mu$ L/min that is usually used for cell adhesion studies, does not allow cells interact extensively with the underlying substrate, thus tracing bulk differences between cells. Cell lines with slight differences could probably differentiate using the given experimental conditions.

Cell adhesion studies were performed on gold surface in the absence of a protein substrate. In these studies, Nthy and ARO cells interacted with gold surface, reached equilibrium and gave high frequency and dissipation signals. In fact, Nthy and ARO yielded a significantly higher QCM-D response on gold rather than of fibrinogen-coated gold (Fig.18, Fig.19). Also, Nthy and ARO binding reactions were led to equilibrium faster on gold surface than on coated surface. All above highlight the crucial role that substrate plays for cell-substrate studies and imply the existence of a specific mechanism that mediates cell binding on fibrinogen.

Based on the above observations, cell adhesion studies were designed using the same conditions on fibrinogen-coated gold. When interacting with fibrinogen, ARO

and Nthy cells generate high frequency and dissipation shifts, which are in most cases proportional to cell concentration (Fig.20, Fig.21). Also, the acoustic ratio value within different concentrations of both cell lines is  $\Delta D/\Delta F \approx 0.01 \cdot 10^{-6}/\text{Hz}$ . All experiments can be summarized to create binding isotherms of cells at pseudo-equilibrium conditions (Fig.22). As cell concentration of ARO and Nthy increase, both frequency and dissipation values increase too. ARO average frequency and dissipation values are lower compared to those of Nthy. Especially for low cell concentrations, ARO exhibit a reduced binding capacity on fibrinogen and cause less energy losses than Nthy. This finding keeps up with the resulting frequency and dissipation shifts as depicted in Figure17. ARO and Nthy cell lines can be distinguished on fibrinogen-coated gold for given experimental conditions even if the binding reaction could not reach equilibrium for the time interval studied. This experiment could be further used as a tool to discriminate various cell lines.

Here it is crucial to report that frequency and dissipation shifts due to cell binding on ECM protein layer, act as the major determinant of QCM-D responses. However, changes in the elastic properties of the ECM proteins at cell-substrate interface play a major role too [10]. The interfacial protein layer directly couples the sensor surface with the cell cytoskeleton via the formation of focal adhesions. Thus, changes inside the cell cytoplasm can be directly transferred to the sensor surface as changes in the viscoelastic cell properties and modify the signals.

Cell adhesion kinetics is determined by the total number of cell surface receptors (related to the cell number) and the interaction of these receptors with ECM ligands. Kinetic analysis of QCM-D frequency data provided us with valuable information for cell adhesion process. Acquired  $\Delta F$  curves can be fitted and described by single exponential decay for both cell lines. The single exponential function dependence suggests that only one-site ligand-receptor binding kinetics might be involved and that cell-cell cooperativity is not crucial for establishment of cell binding [71]. Exponential decay fitting proved that for low cell concentrations and similar theoretical frequency values, ARO exhibit slower adhesion than Nthy on fibrinogen. On the contrary, for high cell concentrations and similar theoretical frequency values both cell lines had similar kinetics (Fig.23). Additionally, adhesion process contained an initial lag phase where frequency values did not obey equation (3). The lag phase was present at low and high cell concentrations. During the lag phase the cell mass is weakly coupled to the sensor surface [71]. Furthermore, there was a need to understand cell adhesion process at conditions approximating equilibrium. In order to correct binding isotherms of Nthy and ARO (Fig.22), where acquired  $\Delta F$  values are indicative of the pseudo-equilibrium QCM-D response, we used equation (3) to approximate equilibrium frequency values. Calculations unraveled a phenomenon: low cell concentrations can easily reach plateau while higher ones cannot, within the

time interval examined (Fig.24). The above suggest that it is meaningful to examine low cell concentrations where kinetics of the two cell lines is different. Although high cell concentrations result in large frequency shifts no kinetic differences are observed. Also, the corrected binding isotherm (Fig.24c) confirmed the aforementioned reduced binding capacity of ARO cells on fibrinogen. Binding isotherms revealed that dissipation change was very sensitive and could be used to differentiate between various cell suspensions [70]. In contrast, frequency change was less sensitive and inconsistent, as monitored in cases of Love-wave device [69]. Also, changes in dissipation represent energy loss at the sensed interface layer which may occur due to various interactions in the cell-surface interface and morphology of bound cells.

Optical microscopy images constitute the visualization of cell adhesion process and contain information regarding the shape and morphology of adhered cells. In general, Nthy appeared as flattened round ( $\approx 50\mu\text{m}$  diameter) and round ( $\approx 20\text{-}40\mu\text{m}$  diameter) cells while ARO appeared as rounded cells with an approximate diameter of  $15\text{-}30\mu\text{m}$ . Indeed, ARO preserve a round morphology that seems more compact than Nthy cells. Nthy cells have higher average contact area than ARO cells, suggesting that they create more focal adhesions on fibrinogen than ARO. Fredriksson et al [57], suggest that frequency changes are proportional to contact area between cell and QCM, and frequency changes can be small for spherical non-spread cells. Moreover, artificial gold surfaces managed to replace commercially available sensor surfaces. The problem was that sensor material hindered light transition so that microscopy observation of the cell-substrate interface was sometimes impossible. Artificial gold surfaces consisted of glass (instead of quartz) covered with chromium and gold thus mimicking surface properties of gold sensors. Observation of cells on artificial gold surfaces through optical microscopy proved simple and comfortable, establishing artificial surfaces as an alternative tool for QCM-D coupled microscopy.

As stated before, comparative analysis of adhesion on gold and fibrinogen-coated gold surfaces (Fig.18, Fig.19) suggested the existence of a specific mechanism that mediates ARO and Nthy adhesion on fibrinogen. Cell adhesion process is driven by ligand-receptor interactions and the major binding events are mediated by integrins [50]. To examine the existence of a molecular mechanism we used RGD peptides which are recognized by the majority of integrins. Firstly, we examined the interaction of RGD peptides with a fibrinogen-coated surface. In Figure28 it is clear that RGDs do not interact with fibrinogen as they cause no changes in frequency or dissipation signals. Then, the interaction of RGDs with cell suspensions was monitored. RGDs incubated with Nthy cells adhered on a fibrinogen-coated sensor and exhibited the same frequency and dissipation signals as Nthy cells (Fig.29). This

implies that RGDs cannot block or reduce Nthy binding on fibrinogen even if they interact with Nthy cells to some extent. Finally, RGD peptides were inserted at the end of a cell adhesion experiment, where ARO cells adhered on fibrinogen-coated gold, but did not manage to detach cells from surface or bind on them. Li et al [34] used cyclic peptide c(RGDfV) to compete integrin-ECM interaction, resulting in cell detachment. Based on the above, these experiments suggest that binding of Nthy and ARO on fibrinogen was not integrin-mediated.

## *CONCLUSION*

---

Protein adsorption studies on gold surface proved to be concentration-dependent for the given experimental conditions. A combination of acoustic ratio measurements with Sauerbrey (eq.2) calculated monolayer coverage provided a great insight on the orientational changes molecules undergo during adsorption process. We suggest that collagen molecules initially adopt a flat orientation on gold surface but for higher molecule densities collagen adopts a more vertical/tilted orientation. Thereupon, we recommend that fibrinogen and fibronectin molecules acquire a tight flat orientation during adsorption on gold surface.

Cell adhesion studies revealed the complexity of cell-substrate interactions as many factors could influence cell adhesion process. These factors include the temperature, flow rate, concentrations of samples, coating protein and substrate used. Firstly, flow rate can alter results of cell adhesion process as for higher flow rates cells interact roughly with the underlying substrate. Then, the coating protein plays a major role for cell adhesion because it links the substrate with cells and can transfer signals inside the cell upon binding. Also, orientation and aggregation state of the substrate can determine cell adhesion fate.

In this study, the adhesion of normal Nthy and malignant ARO cells was monitored on fibrinogen-coated gold sensors. Binding isotherms of ARO and Nthy cells revealed that ARO exhibit a reduced binding capacity on fibrinogen and cause less energy losses than Nthy cells. This can be attributed to the fact that malignant cells are less adherent and more motile than normal cells in order to accomplish metastasis to neighboring tissues. Also, microscopy images proved that ARO cells have a rounded morphology compared to the flattened Nthy ones. This can suggest that Nthy cells make more focal adhesion points on fibrinogen than ARO.

Additionally, these cell lines give distinct signals ( $\Delta F$  and  $\Delta D$  values) and kinetic behaviors for low cell concentrations examined. Especially, low concentrations of ARO cells exhibit a slower adhesion rate than those of Nthy. In contrast, high cell concentrations result in same kinetic behavior. Thus, we assume that low cell concentrations contain all the information needed to distinguish these two cell lines.

Kinetic analysis of QCM-D data calculated the theoretical frequency and dissipation values at equilibrium conditions. Strangely, low cell concentrations reach equilibrium faster than the higher ones. Also, kinetic analysis revealed the presence of a lag phase where cells are loosely bound to the sensor surface.

For the cell lines tested here, the acoustic ratio  $\Delta D/\Delta F$  measurements did not manage to provide us with distinct signatures as in the case of protein adsorption. Finally, the binding of these cell lines on fibrinogen is mediated by an unknown molecular mechanism that needs further examination.

All the aforementioned findings contribute to a better understanding of the in-vitro system examined. As for protein adsorption, attention will be paid to the studying of the structure, composition, thickness and properties of the adsorbed layer. This can be achieved by AFM, Ellipsometry and XPS accompanied by QCM-D technique. Moreover, there is a great pressure for the development of reliable cancer detection techniques for a label-free, high throughput phenotypic of potential cancer cells. Thus, we would like to use more cell lines to search for their signatures on gold and check their metastatic potential. If this is feasibly, the next step will be to test biopsy samples and identify the ratio of malignant versus healthy cells and the propensity of healthy cells to become malignant. In this way, QCM-D can evolve as a powerful diagnostic and prognostic tool replacing the well-established Fine Needle Aspiration technique.

## CHAPTER 5

### REFERENCES

---

- [1] Cooper MA (2006) Non-optical screening platforms: the next wave in label-free screening? *Drug Discov Today* 11: 1068-1074.
- [2] Friedt JM (2003) Combined surface acoustic wave and surface plasmon resonance measurement of collagen and fibrinogen layers. *Biological Physics*, Cornell University Library.
- [3] Nezu T (2010) Viscoelastic adlayers of collagen and lysozyme studied using quartz crystal microbalance with dissipation monitoring. *International Journal of Biological Macromolecules* 46: 396-403
- [4] Cantor CR, Schimmel PR (1980) Part I: The Conformation of Biological Macromolecules. *Biophysical Chemistry* 68: 70–71, 95–100
- [5] Gurdak E (2005) Resolution of the Vertical and Horizontal Heterogeneity of Adsorbed Collagen Layers by Combination of QCM-D and AFM. *Langmuir* 21: 10684-10692
- [6] Gurdak E (2006) Influence of collagen denaturation on the nanoscale organization of adsorbed layers. *Journal of Colloid and Interface Science* 302: 475-484
- [7] Persikov AV (2005) Electrostatic interactions involving lysine make major contributions to collagen triple-helix stability. *Biochemistry* 44(5): 1414-1422
- [8] Kadler KE (1996) Collagen fibril formation. *Biochem J.* 316 (1): 1-11
- [9] Fathima NN (2011) Degree of crosslinking of collagen at interfaces: Adhesion and shear rheological indicators. *International Journal of Biological Macromolecules* 48: 67-73
- [10] Tymchenko N (2012) Reversible Changes in Cell Morphology due to Cytoskeletal Rearrangements Measured in Real-Time by QCM-D. *Biointerfaces* 7: 43
- [11] Ni Y (2011) Characterization of self-assembled decyl bis phosphonate–Collagen layers on titanium by QCM-D and osteoblast-compatibility. *Applied Surface Science* 257: 9287-9292
- [12] Huang CJ (2010) Type I Collagen-Functionalized Supported Lipid Bilayer as a Cell Culture Platform. *Biomacromolecules* 11: 1231-1240
- [13] Lin Q (2011) Heparin/collagen multilayer as a thromboresistant and endothelial favorable coating for intravascular stent. *Journal of Biomedical Materials Research A* 96: 132-141
- [14] Muratsugu M (1997) Adhesion of human platelets to collagen detected by <sup>51</sup>Cr labeling and acoustic wave sensor. *Analytica Chimica Acta* 342: 23-29
- [15] Jawad MA (2009) Fibronectin adsorption studied using neutron reflectometry and complementary techniques. *The European Physical Journal E* 30: 175-179

- [16] Giambianco N (2011) Fibronectin Conformation Switch Induced by Coadsorption with Human Serum Albumin. *Langmuir* 27(1): 312-319
- [17] Steele JG (1995) Adsorption of fibronectin and vitronectin onto Primaria and tissue culture polystyrene and relationship to the mechanism of initial attachment of human vein endothelial cells and BHK-21 fibroblasts. *Biomaterials* 16(14): 1057-1067
- [18] Renner L (2005) Fibronectin Displacement at Polymer Surfaces. *Langmuir* 21: 4571-4577
- [19] Hemmersam AG (2008) Fibronectin adsorption on gold, Ti-, and Ta-oxide investigated by QCM-D and RSA modeling. *Journal of Colloid and Interface Science* 320: 110-116
- [20] Dolatshahi-Pirouz A (2009) Enhanced Surface Activation of Fibronectin upon Adsorption on Hydroxyapatite. *Langmuir* 25: 2971-2978
- [21] Marxer CG (2003) Study of adsorption and viscoelastic properties of proteins with a quartz crystal microbalance by measuring the oscillation amplitude. *Journal of Colloid and Interface Science* 261: 291-298
- [22] Giambianco N (2012) Coadsorption-dependent orientation of fibronectin epitopes at hydrophilic gold surfaces. *Soft Matter* 8: 8370-8378
- [23] Molino PJ (2012) Fibronectin and Bovine Serum Albumin Adsorption and Conformational Dynamics on Inherently Conducting Polymers: A QCM-D Study. *Langmuir* 28: 8433-8445
- [24] Wittmer CR (2007) Fibronectin terminated multilayer films: Protein adsorption and cell attachment studies. *Biomaterials* 28: 851-860
- [25] Pegueroles M (2012) Adsorption of Fibronectin, Fibrinogen, and Albumin on TiO<sub>2</sub>: Time-Resolved Kinetics, Structural Changes, and Competition Study. *Biointerfaces* 7:48
- [26] Lord MS (2008) Extracellular matrix remodelling during cell adhesion monitored by the quartz crystal microbalance. *Biomaterials* 29: 2581-2587
- [27] Huang CJ (2010) Effects of extracellular matrix protein functionalized fluid membrane on cell adhesion and matrix remodeling. *Biomaterials* 31: 7183-7195
- [28] Seo JH (2013) Adsorption state of fibronectin on poly(dimethylsiloxane) surfaces with varied stiffness can dominate adhesion density of fibroblasts. *Acta Biomaterialia* 9: 5493-5501
- [29] Dolatshahi-Pirouz A (2011) Cell shape and spreading of stromal (mesenchymal) stem cells cultured on fibronectin coated gold and hydroxyapatite surfaces. *Colloids and Surfaces B: Biointerfaces* 84: 18-25
- [30] Scheideler L (2007) Photocoupling of fibronectin to titanium surfaces influences keratinocyte adhesion, pellicle formation and thrombogenicity. *Dental Materials* 23: 469-478

- [31] Lord MS (2009) Protein adsorption on derivatives of hyaluronic acid and subsequent cellular response. *Journal of Biomedical Materials Research Part A* 91(3):635-646
- [32] Stachurska A (2011) Interaction of PC-3 cells with fibronectin adsorbed on sulfonated polystyrene surfaces. *Folia Histochemica Et Cytobiologica* 49(4): 706-718
- [33] Lord MS (2006) Monitoring cell adhesion on tantalum and oxidised polystyrene using a quartz crystal microbalance with dissipation. *Biomaterials* 27: 4529-4537
- [34] Li J (2005) Monitoring of integrin-mediated adhesion of human ovarian cancer cells to model protein surfaces by quartz crystal resonators: evaluation in the impedance analysis mode. *Biosensors and Bioelectronics* 20: 1333-1340
- [35] Soumetz FC (2008) Human Osteoblast-Like Cells Response to Nanofunctionalized Surfaces for Tissue Engineering. *Journal of Biomedical Materials Research Part B: Applied Biomaterials* 84(1): 249-255
- [36] Llopis-Hernandez V (2011) Role of Surface Chemistry in Protein Remodeling at the Cell-Material Interface. *PLoS ONE* 6(5): e19610
- [37] Da-Silva AC (2013) Acoustic detection of cell adhesion to a coated quartz crystal microbalance – implications for studying the biocompatibility of polymers. *Biotechnology Journal* 8: 690-698
- [38] Kollman JM (2009) Crystal Structure of Human Fibrinogen. *Biochemistry* 48: 3877-3886
- [39] Hemmersam AG (2005) Adsorption of fibrinogen on tantalum oxide, titanium oxide and gold studied by the QCM-D technique. *Colloids and Surfaces B: Biointerfaces* 43: 208-215
- [40] Guicai L (2008) Investigation of fibrinogen adsorption on solid surface by quartz crystal microbalance with dissipation (QCM-D) and ELISA. *Solid State Ionics* 179: 932-935
- [41] Kirschhöfer F (2013) Quartz crystal microbalance with dissipation coupled to on-chip MALDI-ToF mass spectrometry as a tool for characterizing proteinaceous conditioning films on functionalized surfaces. *Analytica Chimica Acta* 802: 95-102
- [42] Ma C (2013) Protein–protein resistance investigated by quartz crystal microbalance. *Colloids and Surfaces B: Biointerfaces* 104: 5-10
- [43] Dobrzanska DA (2013) Oxidation of Tertiary Amine-Derivatized Surfaces To Control Protein Adhesion. *Langmuir* 29: 2961-2970
- [44] Kao P (2011) Volumetric interpretation of protein adsorption: Interfacial packing of protein adsorbed to hydrophobic surfaces from surface-saturating solution concentrations. *Biomaterials* 32: 969-978
- [45] Berglin M (2009) Fibrinogen Adsorption and Conformational Change on Model Polymers: Novel Aspects of Mutual Molecular Rearrangement. *Langmuir* 25(10): 5602-5608

- [46] Yao C (2013) Detection of Fibrinogen and Coagulation Factor VIII in Plasma by a Quartz Crystal Microbalance Biosensor. *Sensors* 13: 6946-6956
- [47] Evans-Nguyen KM (2005) Fibrin Proliferation at Model Surfaces: Influence of Surface Properties. *Langmuir* 21: 1691-1694
- [48] Sinn S (2011) NCO-sP(EO-stat-PO) Coatings on Gold Sensors—a QCM Study of Hemocompatibility. *Sensors* 11: 5253-5269
- [49] Gugutkov D (2011) Fibrinogen organization at the cell–material interface directs endothelial cell behavior. *Journal of Bioactive and Compatible Polymers* 26(4): 375-387
- [50] Arnaout MA (2007) Structure and mechanics of integrin-based cell adhesion. *Current Opinion in Cell Biology* 19(5): 495-507
- [51] Sivakumar P (2006) New insights into extracellular matrix assembly and reorganization from dynamic imaging of extracellular matrix proteins in living osteoblasts. *Journal of Cell Science* 119(7): 1350-1360
- [52] Ruoslahti E (1986) Arg-Gly-Asp: a versatile cell recognition signal. *Cell* 44(4): 517-518
- [53] Wegener J (1998) Cell adhesion monitoring using a quartz crystal microbalance: comparative analysis of different mammalian cell lines. *Eur. Biophys. J* 28: 26-37
- [54] Hong S (2006) Real-time analysis of cell–surface adhesive interactions using thickness shear mode resonator. *Biomaterials* 27: 5813-5820
- [55] Xi J (2013) Quartz Crystal Microbalance in Cell Biology Studies. *Journal Biochips and Tissue chips* S5: 001
- [56] Sauerbrey G (1959) Verwendung von Schwingquartzen zur Wagung dünner Schichten und zur microwagung. *Z Phys* 155:206–222
- [57] Fredriksson C (1998) In vitro real-time characterization of cell attachment and spreading. *Journal of Materials Science: Materials in Medicine* 9: 785-788
- [58] Rodahl M (1997) Simultaneous frequency and dissipation factor QCM measurements of biomolecular adsorption and cell adhesion. *Faraday Discussions*: 229-246
- [59] Wegener J (2000) Analysis of the composite response of shear wave resonators to the attachment of mammalian cells. *Biophysical Journal* 78: 2821-2833
- [60] Fredriksson C (1998) The piezoelectric Quartz Crystal Mass and Dissipation Sensor: A Means of Studying Cell Adhesion. *Langmuir* (1998) 14: 248-251
- [61] Hayes JS (2012) The Cell-Surface Interaction. *Adv. Biochem. Eng. Biotechnol.* 126:1-31
- [62] Musso R (2013) Differential proteomic and phenotypic behavior of papillary and anaplastic thyroid cell lines. *Journal of Proteomics* 90: 115-125

- [63] Giuffrida D (2000) Anaplastic thyroid carcinoma: Current diagnosis and treatment. *Annals of Oncology* 11: 1083-1089
- [64] Crevoisier R (2004) Combined treatment of anaplastic thyroid carcinoma with surgery, chemotherapy and hyperfractionated accelerated external radiotherapy. *Int J Radiat Oncol Biol Phys* 60: 1137-1143.
- [65] Arcinas A (2009) Cell Surface and Secreted Protein Profiles of Human Thyroid Cancer Cell Lines Reveal Distinct Glycoprotein Patterns. *J Proteome Res* 8(8): 3958–3968
- [66] Tsortos A (2008) Shear acoustic wave biosensor for detecting DNA intrinsic viscosity and conformation: A study with QCM-D. *Biosensors and Bioelectronics* 24: 836-841
- [67] Papadakis G (2010) Acoustic Characterization of Nanoswitch Structures: Application to the DNA Holliday Junction. *Nano Letters* 10: 5093-5097
- [68] Tsortos A (2008) Quantitative Determination of Size and Shape of Surface-Bound DNA Using an Acoustic Wave Sensor. *Biophysical Journal* 94: 2706-2715
- [69] Saitakis M (2010) Probing the interaction of a membrane receptor with a surface-attached ligand using whole cells on acoustic biosensors. *Biosensors and Bioelectronics* 25: 1688-1693
- [70] Saitakis M (2008) Measurement of Two-Dimensional Binding Constants between Cell-Bound Major Histocompatibility Complex and Immobilized Antibodies with an Acoustic Biosensor. *Biophysical Journal* 95: 4963-4971
- [71] Zhou T (2012) Dynamic cell adhesion and viscoelastic signatures distinguish normal from malignant human mammary cells using quartz crystal microbalance. *Analytical Biochemistry* 421: 164-171

## APPENDIX

Nthy 50min adhesion	Concentration (cells/ml)	Average $\Delta F$ (Hz)	Stdev	Average $\Delta D$ (10 <sup>-6</sup> )	Stdev	Average D/f (10 <sup>-6</sup> /Hz)	Stdev	Number of experime nts
	2,00E+04	48,666	5,686	0,5	0,045	0,010293359	0,00025447	3
3,00E+04	94	11,314	1,21	0,353	0,012738258	0,002228047	2	
5,00E+04	139	1,732	1,553	0,101	0,011172923	0,000659382	3	
1,00E+05	115,25	4,787	1,205	0,095	0,010449009	0,00056306	4	
1,50E+05	167,5	4,655	1,862	0,123	0,011128521	0,000857297	4	
2,00E+05	105	10,536	1,03	0,153	0,009814404	0,000541837	3	
ARO 50min adhesion	Concentration (cells/ml)	Average $\Delta F$ (Hz)	Stdev	Average $\Delta D$ (10 <sup>-6</sup> )	Stdev	Average D/f (10 <sup>-6</sup> /Hz)	Stdev	Number of experime nts
	2,00E+04	25	0	0,215	0,035	0,0086	0,001414214	2
3,00E+04	27,666	5,507	0,273	0,094	0,00972583	0,001571216	3	
5,00E+04	29,5	2,887	0,235	0,017	0,007989209	0,000474296	4	
1,00E+05	78	6,633	0,692	0,033	0,008907743	0,000546079	4	
1,50E+05	103,25	13,048	0,975	0,108	0,009514862	0,001289927	4	
2,00E+05	74,666	0,577	0,743	0,065	0,009951952	0,000808785	3	

**Table A. Detailed table summarizing the average  $\Delta F$ ,  $\Delta D$  and  $\Delta D/ \Delta F$  values used in the experiment described in pages 30-32.**

<b>Nthy adhesion</b>	<b>Concentration (cells/ml)</b>	<b>Average <math>\Delta F</math> (Hz)</b>	<b>Stdev</b>	<b>Average <math>\Delta D</math> (10<sup>-6</sup>)</b>	<b>Stdev</b>	<b>Number of experiments</b>
	1,00E+03	-	-	-	-	-
	5,00E+03	388	0	5,105	0,007071068	2
	1,00E+04	337	38,18376618	5,72	0,67882251	2
	3,00E+04	459,5	13,43502884	5,665	0,261629509	2
	5,00E+04	459,5	13,43502884	6,555	0,106066017	2
	1,00E+05	523,5	40,30508653	6,95	0,509116882	2
	1,50E+05	501,5	3,535533906	6,64	0,494974747	2
	2,00E+05	539	25,45584412	6,48	0,353553391	2
<b>ARO adhesion</b>	<b>Concentration (cells/ml)</b>	<b>Average <math>\Delta F</math> (Hz)</b>	<b>Stdev</b>	<b>Average <math>\Delta D</math> (10<sup>-6</sup>)</b>	<b>Stdev</b>	<b>Number of experiments</b>
	1,00E+03	211	28,28427125	2,555	0,176776695	2
	5,00E+03	248	19,79898987	3,38	0,282842712	2
	1,00E+04	338	50,91168825	3,935	1,364716088	2
	3,00E+04	363,5	26,1629509	3,92	0,113137085	2
	5,00E+04	380	52,32590181	5,57	1,046518036	2
	1,00E+05	337	7,071067812	4,385	1,053589104	2
	1,50E+05	384	14,14213562	5,045	0,304055916	2
	2,00E+05	430,5	57,27564928	5,075	1,237436867	2

**Table B. Detailed table summarizing the average  $\Delta F$  and  $\Delta D$  values used in the experiment described in pages 33-34. Data are kindly provided by MSc student Stratiotis Dimitrios.**

<b>Nthy 250min adhesion</b>	<b>Concentration (cells/ml)</b>	<b>Average <math>\Delta F</math> (Hz)</b>	<b>Stdev</b>	<b>Average <math>\Delta D</math> (10<sup>-6</sup>)</b>	<b>Stdev</b>	<b>Number of experiments</b>
	1,00E+04	62,25	31,06311	0,86	0,288329	4
	2,00E+04	102	35,24202	1,254	0,346742	5
	3,00E+04	147,2	17,85217	1,758	0,343686	5
	5,00E+04	173,75	22,45551	1,97	0,342053	4
	8,00E+04	206,5	5,446712	2,515	0,169017	4
	1,00E+05	219,25	4,99166	2,565	0,2002498	4
	1,50E+05	228	28,52367	2,716667	0,363079	6
	2,00E+05	259,25	8,80814	3,1075	0,090323	4
<b>ARO 250min adhesion</b>	<b>Concentration (cells/ml)</b>	<b>Average <math>\Delta F</math> (Hz)</b>	<b>Stdev</b>	<b>Average <math>\Delta D</math> (10<sup>-6</sup>)</b>	<b>Stdev</b>	<b>Number of experiments</b>
	1,00E+04	49,6	10,23719	0,354	0,063087	5
	2,00E+04	65,83333	30,8572	0,561667	0,206632	6
	3,00E+04	84,75	18,57193	0,6375	0,295113	4
	5,00E+04	113	30,46309	0,934	0,57275649	5
	8,00E+04	162,6	32,76126	1,654	0,4358096	5
	1,00E+05	183,6667	22,03028	1,873333	0,315647	3
	1,50E+05	201	25,46894	1,98	0,233381	4
	2,00E+05	235,667	25,0067	2,62	0,40841	3

**Table C. Detailed table summarizing the average  $\Delta F$  and  $\Delta D$  values used in the experiment described in pages 35-37.**

<b>Nthy corrected</b>	<b>Concentration (cells/ml)</b>	<b>Average <math>\Delta F</math> (Hz)</b>	<b>Stdev</b>	<b>Number of experiments</b>
	1,00E+04	95,5	9,19	2
	2,00E+04	148	28,74	3
	3,00E+04	179,66	31,94	3
	5,00E+04	214,66	28,18	3
	8,00E+04	304,5	2,12	2
	1,00E+05	285,75	26,24	4
	1,50E+05	336	36,75	3
	2,00E+05	319	20,01	4
<b>ARO corrected</b>	<b>Concentration (cells/ml)</b>	<b>Average <math>\Delta F</math> (Hz)</b>	<b>Stdev</b>	<b>Number of experiments</b>
	1,00E+04	92	14,73	3
	2,00E+04	89	34,07	3
	3,00E+04	92,5	0,7	2
	5,00E+04	224	38,03	3
	8,00E+04	357,33	32	3
	1,00E+05	208	0	1
	1,50E+05	284,5	61,51	2
	2,00E+05	275,33	9,01	3

**Table D. Detailed table summarizing the average  $\Delta F$  values used in the experiment described in pages 38-40.**